Wave energy extraction for an array of dual-oscillating wave surge converter with different layouts

Yong Cheng[a], Chen Xi[a], Saishuai Dai[b,*1], Chunyan Ji[a], Margot Cocard[b]

[a]*School of naval architecture and ocean engineering, Jiangsu University of Science and Technology, Zhenjiang, 212003, China*

[b]*University of Strathclyde, Naval Architecture, Ocean and Marine Engineering Department, Glasgow, United Kingdom*

Abstract

Array configuration of oscillating wave surge converter (OWSC) devices in nearshore is a preferable option for realizing a cost-balance of extracting wave energy and reducing installation expense due to closer installed place to coastline ("shorter weather windows and" has been deleted). The goal of the present work is to assess energy extraction of an array of dual-OWSC system with different layout schemes in comparison with an isolated OWSC, which can be regarded as a guideline for multi-array configuration in realistic wave farm. The coupled three-dimensional (3-D) hydrodynamic model is established based on the potential flow theory with fully nonlinear boundary condition in time domain. A non-dimensional approach is conducted to focusing on the accurate effects of multi-body interaction, wave nonlinearity, wave resonance, mechanical damping, layout scheme and oblique incidence as optimization design. For a front-back array system, wave resonance in dual-module gap enhances significantly the energy extraction of the front OWSC but does not contribute much to that of the back OWSC. Furthermore, wave resonance in wide gap has a positive effect on the capture efficiency in large wave periods. An in-line array system has a beneficial performance in small wave periods, while a staggered array system realizes more energy extraction in resonance region. A strong wave disturbance between flap sides of an in-line and staggered system, leads to the increase of energy extraction for the back OWSC with imposing small incident wave heading. Therefore, the combination of multi-triple-array OWSC with different gap distances will provide a desirable configuration which is independent on oblique wave conditions.

Keywords

Array configuration, oscillating wave surge converter, wave resonance, wave energy extraction, fully nonlinear simulation, oblique waves

1 Introduction

To cope with the unsustainable use of fossil energy and environment pollution caused by extensive use of fossil energy, some renewable energies such as wave, wind, tide and solar power are gradually utilized to supply an estimated 7% of global electricity production by the end of 2050 [1]. Among these renewable energies, wave energy is a huge, largely untapped ocean energy resource, and is very attractive option due to its high energy density and friendly environmental factors. It is common ("a historic statement" has been revised as "common") that the nearshore wave energy resource is significantly less than that at deep water. However, this belief is commonly based on the omnidirectional or gross wave energy resource, which is only appropriate for some isolated

*Corresponding author: Saishuai Dai, mainly research in hydrodynamic performance of marine energy devices
E-mail: saishuai.dai@strath.ac.uk

axis-symmetric heaving buoys. Actually, the mean value of the directionally resolved incident wave energy which is defined as the exploitable wave energy resource is a more realistic measure [2]. Based on such a new definition, there are only 10-20% energy losses from the offshore to the nearshore. In addition, the installation and maintenance costs at nearshore are lower due to closer location to the coastline and shorter weather window. In this regard, a wide variety of wave energy converters (WECs) designed for shoreline have been developed, in which the oscillating wave surge converter (OWSC) devices are becoming most popular one due to its mechanical and structural simplicity [3]. Yet the hydrodynamic behavior of multi-OWSC devices remains not well-understood due to some important factors, i.e. gap resonance, array layout, wave nonlinearity, 3-D flow-field effect, power take-off (PTO) system and oblique wave incidence. The effects of nonlinear multi-body hydrodynamic interaction on the extracted energy of OWSC devices are especially complicated. Further nonlinear hydrodynamic performance of an array of OWSCs should be investigated systematically.

Extensive investigations have been performed using linear wave theory on hydrodynamic performance of an array of OWSCs. Based on the velocity potential model, Sarkar et al. [4] developed an analytic solution by using eigen-function expansion method and obtained wave energy farm of OWSCs in oblique waves. Along the same lines, Noad and Porter [5] analyzed the optimal layouts and spacing among multi-OWSCs and studied the scheme that could enhance the wave energy extraction. It was found that both a 'bowl'-like or a 'chevron' configuration for multi-OWSC devices can amplify the highest efficiency captured by single elements. Renzi and Dias [6] developed a semi-analytical method based on inviscid flow assumption to study the energy extraction performance of an infinite in-line array of OWSC devices, showing that unlike a line of heave-type WECs, an in-line array of flap-type WECs can exploit resonance of the transverse modes to obtain high capture efficiency. However, the drawback of above analytic method is that only simple layouts and geometries are tractable. Thus, Renzi et al. [7] presented a fully numerical frequency-domain model using the finite element method (FEM) based the commercial software COMSOL, and studied the near-resonant phenomenon of the in-line array performance of dual-OWSC by comparison with semi-analytic solutions. Greenwood et al. [8] modeled the wave climate around an in-line array of OWSC system using Boussinesq method and Spectral method, respectively. The Boussinesq method was found to be computationally efficient and more accurate to consider the diffraction effect and directional sensitivity on the energy extraction of OWSCs compared to the Spectral method. Sarkar et al. [9] put forward a machine learning algorithm derived from Gaussian process regression trained with an active learning strategy to study the wave energy conversion of dual-WEC cluster, and arbitrary bathymetry and space constraints were also considered in the determination of optimal layouts. Liu et al. [10] performed a numerical study of the energy conversion of an array of OWSC system using a Gaussian-function-based analytical wake model. The results revealed that the energy output of the staggered layout of OWCSs can be enhanced significantly with narrow and wide OWSCs located in the front and back of wave farm, respectively. Nguyen et al. [11] adopted a finite element-boundary element (FE-BE) hybrid method to investigate the reduction of hydroelastic response and the wave energy extraction of an integrated system including dual-OWSC and a pontoon-type very large floating structure (VLFS). The results showed the synergy between extracting wave energy extraction and reducing hydroelastic response. Tay and Venugopal [12] applied first-order boundary element method (BEM) to simulate the hydrodynamic behavior of an array of OWSCs under irregular multi-directional waves. Although

these mentioned studies provide significant efforts to investigate the hydrodynamic performance of an array of OWSC ("OWCS" has been revised as "OWSC") devices at theoretically and numerically, the fully nonlinear multi-body interaction is ignored which leads to over-predicted wave energy extraction.

Recently, researchers have also developed various nonlinear numerical models ("model" has been revised as "models") based on the Navier-Stokes equations or potential flow theory to analyze an OWSC device. For example, Wei et al. [13] used CFD package ANSYS FLUENT to study the flow characteristics around an OWSC device, which was experimentally studied by Henry et al. [14]. It is found that the viscous effects on the rotational motion are slight for wide flaps. Brito et al. [15] applied the combined model of smoothed particle hydrodynamics (SPH) and multibody interaction to study the transient effect of mechanical constraint induced by PTO system on wave energy extraction of an OWSC device. Mottahedi et al. [16] developed a 2-D CFD model based a fast fictitious domain method and the volume-of-fluid (VOF) method to study the hydrodynamic performance of an OWSC device within the frame of a fixed Eulerian grid. The results indicated that a larger wave amplitude leads to a higher PTO damping coefficient at which the maximum capture efficiency occurs. Dias and Vanden-Broeck [17] investigated the slamming response induced by the OWSC flap hitting free water surface with high speed and found that a jet develops rapidly along the body surface and then enters into the water domain under gravity effect. Later, Sun et al. [18] adopted a domain decomposition method to deal with the overlapping problem of the jet falling into water domain. Based on the time-domain potential model with fully nonlinear boundary conditions, Cheng et al. [19] analyzed the solitary wave slamming on an OWSC device, revealing that the jet flow is much harder to detach from the body surface compared regular wave cases. Cheng et al. [20] further extended the two-dimensional (2-D) method to investigate the effect of local varying topography on the hydrodynamic performance of an OWSC device. Compared with the flat sea-bottom, the variable depth bottom induces some higher-order waves which may lead to higher wave energy extraction near resonant period. ("Dias and Vanden-Broeck [11] , Sun et al. [12] and Cheng et al. [13 and 14] presented time-domain potential model with fully nonlinear boundary conditions to simulate the motion of the free jet surface along body surface of an OWSC device, and adopted the domain decomposition method to deal with the overlapping problem of the jet falling into water domain." has been revised as "Dias and Vanden-Broeck [11] investigated the slamming response induced by the OWSC flap hitting free water surface with high speed and found that a jet develops rapidly along the body surface and then enters into the water domain under gravity effect. Later, Sun et al. [12] adopted a domain decomposition method to deal with the overlapping problem of the jet falling into water domain. Based on the time-domain potential model with fully nonlinear boundary conditions, Cheng et al. [13] analyzed the solitary wave slamming on an OWSC device, revealing that the jet flow is much harder to detach from the body surface compared regular wave cases. Cheng et al. [14] further extended the two-dimensional (2-D) method to investigate the effect of local varying topography on the hydrodynamic performance of an OWSC device. Compared with the flat sea-bottom, the variable depth bottom induces some higher-order waves which may lead to higher wave energy extraction near resonant period."). Then, Cheng et al. [21] developed a time-domain model with viscous correction in motion equation to investigate the energy capture efficiency of a fully submerged OWSC device, showing numerically that the larger wave amplitude would enhance the capture efficiency due to generation of higher order free wave components. Above studies have focused on the nonlinear hydrodynamic behavior of single OWSC

device, and have neglected nonlinear coupling effects between dual OWSC devices, which is one of the important differences between the array of OWSC system and the single OWSC device. Furthermore, there has been few researches to date on the nonlinear hydrodynamics of the array of OWSCs with different layouts.

Nonlinear coupled multi-body interaction is a feature of array of WECs and has an obvious effect on wave energy extracted efficiency. Babarit [22] reviewed the multi-body interaction and the park effect, which can be regard as a function of the number of WECs and the gap between them. Li and Zhang [23] calculated the wave resonance in the narrow gap between two heaving-buoy WECs using a fully nonlinear time-domain model based the potential theory. The results revealed that the buoy draft has a strong effect on maximum capture efficiency and the motion of the inner free surface in gap become stronger ("more violent" has been revised as "stronger") with increasing relative width of the WECs. Kara [24] conducted a numerical study of the wave energy extraction of an array system using truncated vertical cylinder WECs. They found that energy extraction in sway motion for fixed separation distance and incident wave angle is much higher than that in heave motion and has a wider frequency bandwidth of the efficiency magnitude. Nielsen et al. [25] investigated the optimal feedback control of an array of nonlinear wave energy point converters and found that the hydrodynamic calculation requires a finer mesh scheme at a higher wave frequency. Wei et al. [26] analyzed the hydrodynamics, energy extraction and optimal layout of an array of point absorbers using a nonlinear frequency domain model. The results indicated that the large dense layout for an array of WECs leads to destructive effects on the overall energy extraction and this negative effect becomes more prominent at high wave frequency. Wolgamot et al. [27] illustrated the near-trapped phenomenon which can enhance the opportunity for strong multi-body interaction between an array of WECs based on second-order perturbation theory. Michele and Renzi [28] also adopted this numerical model with BEM to investigate hydrodynamic interactions of an array of curved flap-type OWSCs and obtained that when the incident wave direction is perpendicular to the layout of WECs, the differences between the single OWSC and the array were small ("slight" has been revised as "small") on the energy extraction. However, the perturbation model is valid only for incident wave with small amplitude, which ignores the instantaneous motions of both free surface and floating bodies. Zhang et al. [29] established a 2-D nonlinear numerical wave flume based on N-S equations with viscous effects in flow to investigate wave interaction with an integrated system of a floating breakwater and a heaving-buoy type WEC, and then optimized the bottom shape of the WEC at the weather side. These numerical methods developed to study the energy extraction of array of WECs, are based on partial nonlinear boundary conditions. However, the fully nonlinear studies on WECs are still limited, especially those on the effects of wave nonlinearity, large body motion and multi-body interaction on the hydrodynamic behavior of array of WECs. Furthermore, no sufficient attention has been paid to fully nonlinear hydrodynamics of near-shore array of WECs i.e. OWSCs. The nonlinear shoaling effect can induce super-harmonic harmonic waves which modify the wave spectrum in real sea condition because a significant part of the incident wave energy can be exchanged between fundamental waves and higher frequencies. The wavelength of the higher-order waves is generally shorter than that of incoming waves, and the wave amplitude increases with incoming wave amplitude. Such higher-order waves may debase sailing condition and do harm to the safety of OWSC devices. ("The nonlinear shoaling effect can induce super-harmonic harmonic waves which modify the wave spectrum in real sea condition and do harm to the safety of OWSC devices." has been revised as "The nonlinear shoaling effect can induce super-

harmonic harmonic waves which modify the wave spectrum in real sea condition because a significant part of the incident wave energy can be exchanged between fundamental waves and higher frequencies. The wavelength of the higher-order waves is generally shorter than that of incoming waves, and the wave amplitude increases with incoming wave amplitude. Such higher-order waves may debase sailing condition and do harm to the safety of OWSC devices.")

It is not possible to infer the effect of multi-body hydrodynamic interaction on the energy extraction of the dual-OWSC system with different array layouts from existing studies. The motivation and novelty of this paper is twofold; firstly to develop an accurate time-domain three-dimensional (3-D) hydrodynamic model to optimize the design and configuration of a front-back array of dual-OWSC system, and secondly to compare the energy extraction performance of an front-back array system, an in-line array system and a staggered array system. This will help lead to efficiency-enhancing multi-array configuration in realistic wave farm, which broadens the effective bandwidth of energy extraction.

In this work, a 3-D potential flow model based on the time-domain higher-order boundary element method (HOBEM), is developed to investigate the hydrodynamic performance of an array of OWSC devices. The primary objective of this paper is to elucidate the fully nonlinear mechanism behind extracted wave energy process of an array of dual-OWSC system. The effects of wave nonlinearity, multi-body interaction, wave resonance, layout scheme and incident wave direction on the capture efficiency of the array of OWSCs are systematically investigated. The rest of the present work is arranged as follows: the numerical model is detailedly described in Section 2. Section 3 gives the validations of the numerical model by comparing with the existing results. Then, the nonlinear numerical results are discussed in Section 4. Finally, the conclusions of this work are summarized in Section 5.

2 Mathematical model

2.1 Water integral equation

To accurately simulate the hydrodynamic performance of an array of OWSC devices, the fully nonlinear theory for wave interaction with floating structure is applied as shown in Fig. 1. The space-fixed Cartesian coordinate system $Oxyz$ and each body-fixed coordinate system $O_ix_iy_iz_i$ (i denotes the i-th OWSC) are chosen to describe the relationship fluid and body. Each OWSC device has the same geometrical and mechanical parameters. All terms are non-dimensional according to the water density ρ, the acceleration due to gravity g, and the vertical distance h_1 from the hinged point to calm water surface. Based on the assumption of incompressible, inviscid and irrotational water, the velocity potential Φ which includes the incident part Φ_I and scattering part Φ_R ("Φ_S" has been revised as "Φ_R"), i.e. $\Phi=\Phi_I+\Phi_R$, satisfies the governing equation with Laplace condition. The initial condition during time-domain simulation is undisturbed, and the corresponding boundary conditions incorporates impermeable seabed surface condition, radiation condition at far field, and following fully nonlinear free surface and body surface conditions:

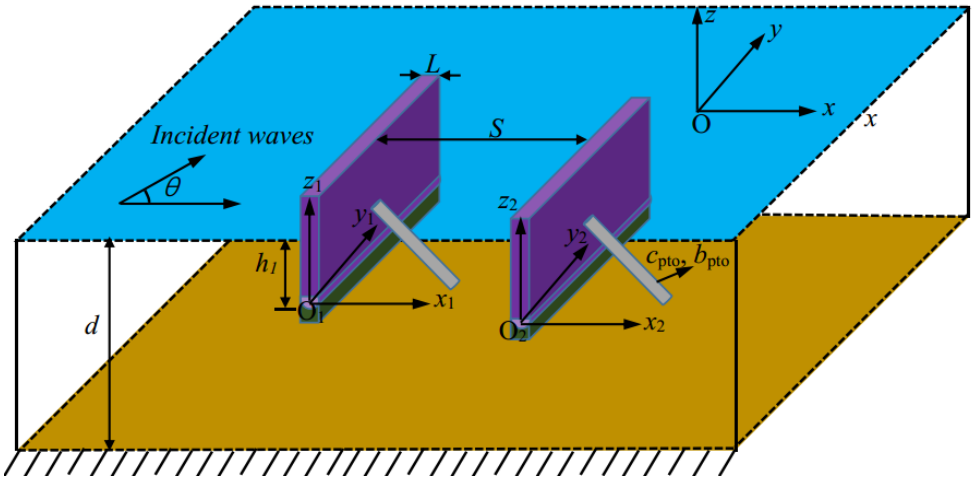

Fig. 1. Coordinate system and sketch of oblique waves interact with an array OWSC system

$$\begin{cases} \dfrac{d(x,y)}{dt} = \dfrac{\partial \Phi_R}{\partial (x,y)} + \dfrac{\partial \Phi_I}{\partial (x,y)} - \nu(r)\left[(x,y) - (x_0,y_0)\right] \\ \dfrac{d\eta_R}{dt} = \dfrac{\partial \Phi_R}{\partial z} + \dfrac{\partial \Phi_I}{\partial z} - \dfrac{\partial \eta_I}{\partial z} - \nabla\Phi_I \cdot \nabla \eta_I - \nabla\Phi_R \cdot \nabla \eta_I - \nu(r)\eta_R \,] \quad \text{on free surface} \\ \dfrac{d\Phi_R}{dt} = \dfrac{1}{2}\left|\nabla\Phi_R\right|^2 - \dfrac{1}{2}\left|\nabla\Phi_I\right|^2 - \dfrac{\partial \Phi_I}{\partial t} - (\eta_I + \eta_R) - \nu(r)\Phi_R \end{cases} \tag{1}$$

where η is free surface elevation, $\nu(r)$ denotes the damping coefficient which absorbs the scattering waves induced by the floating body at far field and has been defined in Ref [30].

$$\frac{\partial(\Phi_R + \Phi_I)}{\partial n} = \ddot{\gamma}^m \cdot (x n_y - y n_x)^m \tag{2}$$

where superscript m denotes the m-th OWSC device; $\boldsymbol{n}=(n_x, n_y, n_z)$ is defined as the unit normal vector of the flap surface; γ^m is the angle displacement of the m-th OWSC device.

Then, the water integral equation based above boundary value problem can be obtained using the Green's theory, and is discretized using a series of eight-node quadratic isoparametric elements:

$$\begin{aligned} &\chi(p_s)\phi(p_s) - \sum_{j=1}^{N_{e2}} \int_{-1}^{1}\int_{-1}^{1} \frac{\partial G}{\partial n} \sum_{v=1}^{8} \Phi_{R(v)} h_v(\xi,\eta) J(\xi,\eta) d\xi d\eta + \sum_{j=1}^{N_{e1}} \int_{-1}^{1}\int_{-1}^{1} G \sum_{e=1}^{8} \frac{\partial \Phi_{R(v)}}{\partial n} h_v(\xi,\eta) J(\xi,\eta) d\xi d\eta = \\ &+ \sum_{j=1}^{N_{e1}} \int_{-1}^{1}\int_{-1}^{1} \frac{\partial G}{\partial n} \sum_{v=1}^{8} \Phi_{R(v)} h_v(\xi,\eta) J(\xi,\eta) d\xi d\eta - \sum_{j=1}^{N_{e2}} \int_{-1}^{1}\int_{-1}^{1} G \sum_{v=1}^{8} \frac{\partial \Phi_{R(v)}}{\partial n} h_v(\xi,\eta) J(\xi,\eta) d\xi d\eta \end{aligned} \tag{3}$$

where Ne_1 and Ne_2 denote the element number on the free surface and body surface, respectively; χ is solid angle coefficient which is decided according the relative location between field point q_f and source point p, and is defined in Ref. [31]; J is the Jacobian matrix; ξ and η are local intrinsic coordinate of each element surface; h is quadratic shape function; G is the Green function which is given by a simple Rankine source and its image with respect to seabed.

2.2 Motion equations of multi-OWSC

Under wave action, each OWSC rotates forth and back about its hinged line and has angular ("angle" has been revised as "angular") displacement only. Thus, the equation of motion for the m-th OWSC can be given

$$I^m \ddot{\gamma}^m + b_{pto}^m \dot{\gamma}^m + c_{pto}^m \gamma^m = M^m \tag{4}$$

where I^m, b^m_{pto}, and c^m_{pto} denote the rotational inertia, the PTO damping, and PTO stiffness of the m-th OWSC, respectively. The wave force moment M^m is calculated by integrating the fluid pressure over the instantaneous wetted surface,

$$M^m = -\iint_{S_B^m} \left(\frac{\partial \Phi}{\partial t} + \frac{1}{2}\left|\nabla \Phi\right|^2\right) \cdot (xn_z - zn_x)^m dS - \iint_{S_B^m} (z-h)^m \cdot (xn_z - zn_x)^m dS + C^m z_c^m \sin\gamma \tag{5}$$

where C^m is the m-th OWSC mass and z^m_c is the initial vertical position of gravity center. The temporal derivative of the velocity potential i.e. $\partial\Phi/\partial t$ is commonly calculated by using backward finite difference method in linear wave-structure interaction. However, for fully nonlinear problem, this backward finite difference method will induce the numerical instability and divergence due to the instantaneous motion of wetted body surface. Therefore, in this paper, some auxiliary functions which satisfy the same governing equation and the corresponding boundary conditions, are introduced to decouple the mutual motion of floating body and fluid flow. The temporal derivative of the velocity potential can be written

$$\frac{\partial \Phi}{\partial t} = \ddot{\gamma}^m \cdot \psi_1^m + \psi_2^m \tag{6}$$

where ψ_1^m and ψ_2^m are auxiliary functions which can be obtained using HOBEM similar to numerical solution of velocity potential. By assembling the coupled (“couple” has been revised as “coupled”) body-fluid Eqs. (4)-(6), the motion equation of the m-th OWSC device can be obtained

$$\left(I^m + a^m\right) \cdot \ddot{\gamma}^m + b^m_{pto} \dot{\gamma}^m + c^m_{pto} \gamma^m = M^m_p \tag{7}$$

where

$$M^m_p = -\iint_{S_B^m} \left(\psi_2^m + \frac{1}{2}\nabla\Phi\cdot\nabla\Phi + z^m - h^m\right) \cdot (xn_z - zn_z)^m dS + C^m z_c^m \sin\gamma^m \tag{8}$$

$$a^m = \iint_{S_B^m} \psi_1^m \cdot (xn_z - zn_x)^m dS \tag{9}$$

2.3 Wave energy extraction

The nonlinear multi-body interaction affects the hydrodynamic performance of each OWSC device, which can break the barrier of the highest possible efficiency from linear wave theory. In this paper, the average generated power E^m_p at wave period T produced by the m-th OWSC is derived as

$$E^m_p = \frac{1}{C^m T}\int_t^{t+lT} M^m \dot{\gamma}^m dt = \frac{b_{\text{pto}}}{iT}\int_t^{t+lT} \dot{\gamma}^2 dt \tag{10}$$

where $l \geq 1$ is the integer. The oscillatory motion of the m-th OWSC can be given in the series form

$$\gamma^m = \text{Re}\left(\sum_{n=0}^{\infty} \gamma^m_n e^{in\omega t}\right) \tag{11}$$

where γ^m_n is complex amplitude for n-th oscillation frequency $n\omega$. Then, substituting Eq. (11) into (10), we have (detailed process is shown in Appendix A)

$$E_p^m = \frac{1}{2} b_{pto}^m \omega^2 \sum_{n=1}^{\infty} (n|\gamma_n^m|)^2 \tag{12}$$

For an array of OWSC devices, the total generated power E_p can be expressed as

$$E_p = \sum_{m=1}^{M} E_p^m \tag{13}$$

To quantify the effects of multi-body hydrodynamic interaction on the wave energy extraction in the array, the mean interaction factor q_{mean} which is regarded as the ratio of the total generated power of the array and M times generated power from single isolated OWSC, is defined as [27]

$$q_{\text{mean}} = \frac{E_p}{M \times E_{\text{isolated}}} \tag{14}$$

where E_{isolated} is the average generated power of an isolated OWSC. When $q_{\text{mean}}>1$, multi-body hydrodynamic interaction is called as positive interaction, which means that extracted wave energy by the array is higher than that by an isolated WEC. Conversely, when $q_{\text{mean}}<1$, multi-body effect is called as destructive interaction.

Moreover, in order to measure the effect of multi-body hydrodynamic interaction on wave energy extraction of each OWSC, the individual interaction factor q_{ind}^m for m-th OWSC is defined as

$$q_{ind}^m = \frac{E_p^m}{E_{\text{isolated}}} \tag{15}$$

Based on the conservation of energy, the incident wave energy E_w within one wave period T is described

$$E_w = \frac{\lambda}{T^2} \int_0^T \int_{-B/2}^{B/2} \int_{-l}^{\eta_1(0,t)} \Phi_{\text{Ix}} \cdot \Phi_{\text{Ix}} dz dy dt \tag{16}$$

where λ is wavelength. Therefore, the capture efficiency R of the array of OWSC can be determined as the ratio of the extracted power to the wave power

$$R = \frac{E_p}{E_w} \tag{17}$$

3 Convergence and model validation

In the present work, the fifth-order Stokes waves are adopted as the incoming waves, and the corresponding velocity potential and wave elevation can be defined as

$$\Phi_I = \frac{\omega}{(k_5)^2} \sum_{n=1}^{5} (\Phi_I)_n \cosh\left[nk_5(z+d)\right] \sin\left[n(k_5 x - \omega t)\right] \tag{18}$$

$$\eta_I = \frac{1}{k_5} \sum_{n=1}^{5} (\eta_I)_n \cos\left[n(k_5 x - \omega t)\right] \tag{19}$$

where

$$\begin{cases}(\Phi_I)_1 = \Lambda A_{11} + \Lambda^3 A_{13} + \Lambda^5 A_{15} \\ (\Phi_I)_2 = \Lambda^2 A_{22} + \Lambda^4 A_{24} \\ (\Phi_I)_3 = \Lambda^3 A_{33} + \Lambda^5 A_{35} \\ (\Phi_I)_4 = \Lambda^4 A_{44} \\ (\Phi_I)_5 = \gamma^5 A_{55}\end{cases} \tag{20}$$

$$\begin{cases}(\eta_I)_1 = \Lambda \\ (\eta_I)_2 = \Lambda^2 B_{22} + \Lambda^4 B_{24} \\ (\eta_I)_3 = \Lambda^3 B_{33} + \Lambda^5 B_{35} \\ (\eta_I)_4 = \Lambda^4 B_{44} \\ (\eta_I)_5 = \Lambda^5 B_{55}\end{cases} \tag{21}$$

and k_5 is wavenumber obtained from the fifth-order Stokes wave theory [32]. The detailed definitions for Λ, A_{lj} and B_{lj} haven been given by Fenton [32].

3.1 Convergence

A front-back array of dual-OWSC system, a typical case of the present work, was selected to conduct convergent tests for mesh and time step. The OWSC model used for the numerical simulation is a 1:40 scale model described by Henry et al. [14] in a flume. The geometric parameters are identical between two OWSCs with mass m_a=4.269 kg, rotational inertia I=0.1508kg*m^2, thickness L=0.0875 m, width B=0.646 m and the hinged position h_1=0.205 m. The simulated water depth is d=0.305 m, and the PTO mechanical coefficients are set as c_{pto}= 17.308 N*m/radian and b_{pto}=2.503 N*m*s/radian. Above corresponding dimensionless values are m_a=0.49, I=0.42, L=0.42, B=3.15, d=1.49, b_{pto}=1.0 and c_{pto}=1.0, respectively. A sufficiently large computational domain is defined as $10\lambda \times 5\lambda \times d$ (λ denotes incident wavelength and is obtained from dispersion equation) along x, y and z direction. Three different mesh schemes are implemented ("carried out" has been revised as "implemented"), where mesh a denotes $\triangle x = \triangle y = \lambda/15$ on free surface, fifty-five elements along the horizontal circumferential direction on the body surface and twenty elements along the vertical direction, and mesh b and c adopt finer and coarser elements on the free surface, i.e. $\triangle x = \triangle y = \lambda/30$ in mesh b and $\triangle x = \triangle y = \lambda/7$ in mesh c. Fig. 2 shows the time series of rotational angle of each OWSC with three mesh schemes for non-dimensional wave period T=10.76 and wave height H_I=0.18. Here, the time step is set as dt=T/60. It can be obtained from this figure that although the motion responses of the back OWSC match well with each other for mesh a, b and c, there exists an amplitude difference of the front OWSC between mesh a/b and c larger than 5%. Only slight differences of the front OWSC between mesh a and b smaller than 3% can be found in Fig. 2 (a). This indicates that the mesh convergence can be achieved by performing the mesh a scheme. Furthermore, three different time steps dt= T/80, T/60 and T/40 is used to conduct temporal convergent tests, as shown in Fig. 3. The results reveal that the response differences of each OWSC including amplitude difference and phase difference for dt= T/80 and T/60 are smaller than 3%, but the amplitude difference of the front OWSC is larger than 5% for dt= T/40. Therefore, the mesh a scheme with dt=T/60 is applied in the following simulation.

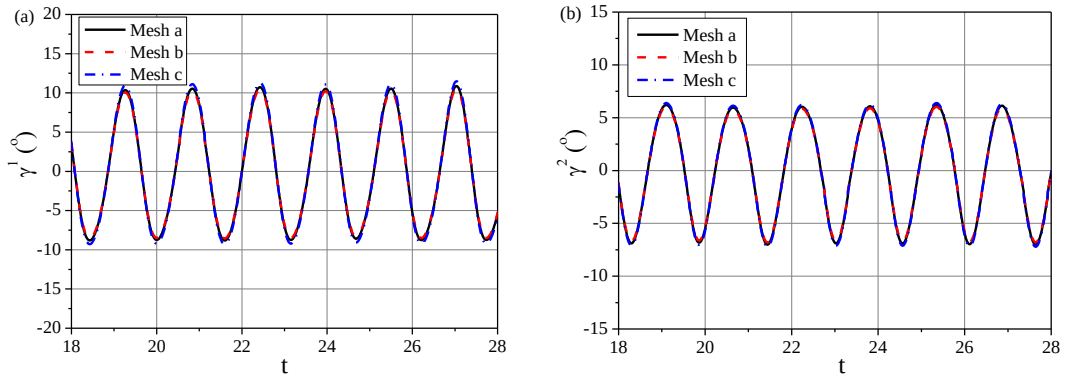

Fig. 2. Convergence tests of motion responses for (a) the front OWSC and (b) the back OWSC with different mesh schemes

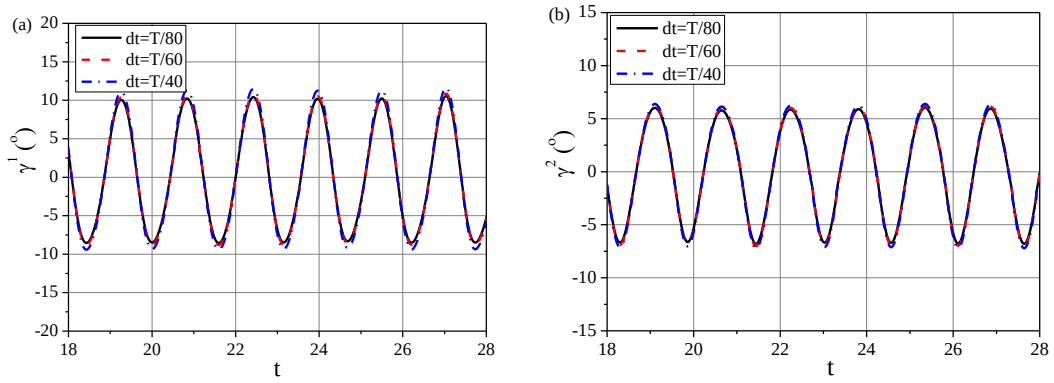

Fig. 3. Convergence tests of motion responses for (a) the front OWSC and (b) the back OWSC with different time steps

3.2 Comparison with analytical solution

To verify the accuracy of the present numerical model, a system of two identical in-line OWSCs by Renzi et al. [7] is simulated. Each OWSC with same width B=26 m and thickness L=2 m is hinged at the location h_1=9 m. The OWSC-OWSC spacing of S=30 m and the water depth d=13 m are considered. All terms are dimensional in order to compare with published results. According linear wave theory, when the natural frequency of the OWSC is close to the wave frequency and the PTO damping coefficients b_{pto} is set as optimal damping coefficient, the capture efficiency can reach its highest value. Thus, the PTO stiffness coefficient c_{pto} is adjusted to meet the resonant requirement, while PTO damping coefficients b_{pto} is set as

$$b_{pto} = \sqrt{\frac{((I + a_z)\omega^2 - (c_{pto} + c_z))^2}{\omega^2} + b_z^2} \tag{22}$$

where a_z and b_z are added mass and radiation damping, respectively. Fig. 4 shows the maximum wave force moment M^m and the motion amplitude factor $D^m{}_\gamma$ for m-th OWSC as function of wave period T for incident wave amplitude A_I=1.0 m. The comparison with the analytical solutions from Renzi et al. [7] is also given in the figures. Here, motion amplitude factor $D^m{}_\gamma$ is defined as the ratio of the maximum horizontal displacement of the OWSC device and wave amplitude:

$$D_\gamma^m = \frac{\tan\left[\max \gamma^m\right] \cdot h}{A_I} \tag{23}$$

The wave direction is chosen to be perpendicular to the layout line of OWSCs, which indicates $M^{m}=M^{1}=M^{2}$ and $D^{m}{}_{\gamma}= D^{1}{}_{\gamma}= D^{2}{}_{\gamma}$. It can be seen from these figures that the present solutions correlate well with the published analytical solutions within whole tested wave period, thereby validating the numerical model.

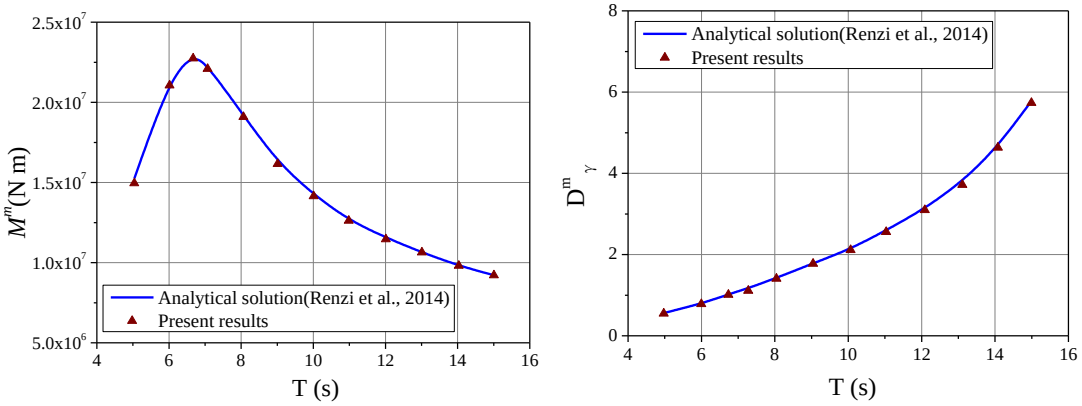

Fig. 4. Comparison of the present results including (a) force moment and (b) motion factor with the analytical solutions by Renzi et al. [7]

3.3 Comparison with experimental data

Furthermore, the 3-D nonlinear numerical solutions are compared with the existing experimental data tested by Henry et al. [14], and the detail parameters have been described in Section 3.1. Here, a regular incident wave with dimensional A_I=0.1 m and T=1.9 s is used to interact with the OWSC device, and mechanical coefficients are set as b_{pto}=c_{pto}=0. Fig. 5 (a) and (b) shows the time series of water surface elevation at the upstream point (-0.9m, 0 m, 0 m) and downstream point (0.9 m, 0 m, 0 m) of the flap, respectively. Fig. 5 (c) shows the comparison of rotating angle. All terms in this sub-section are dimensional in order to compare with published experimental data. It can be seen from these figures that the experimental data can be reproduced well by the numerical solution, especially near the nonlinear time region. On the basis of above comparison, the developed 3-D nonlinear potential flow model has been validated to be accurate enough.

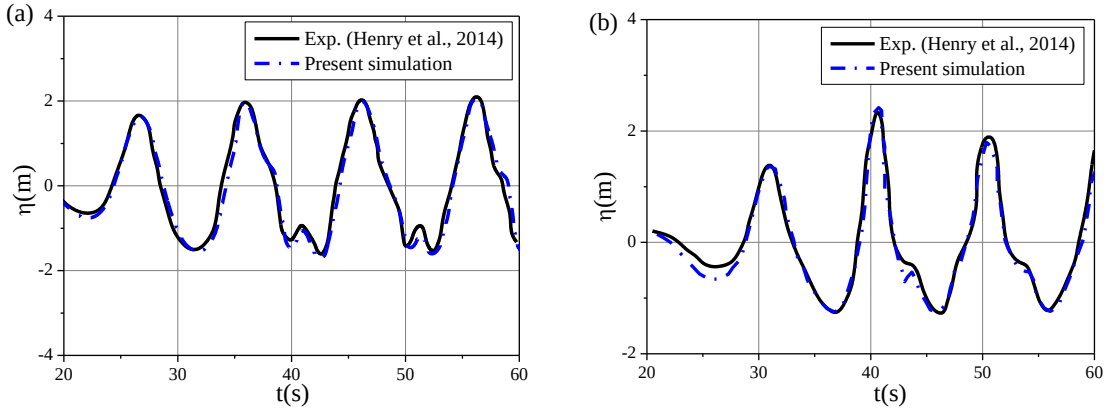

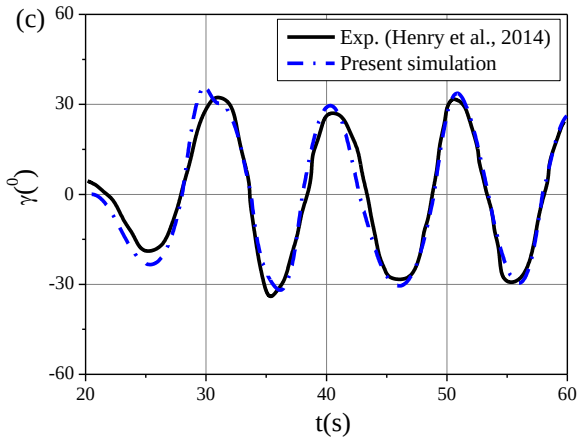

Fig. 5. Time series of (a) water surface elevation with 0.9 m from the weather side of the OWSC, (b) water surface with 0.9 m from the lee side of the OWSC and (c) rotating displacement of the OWSC in comparison with the experimental data in Henry et al. [14]

4 Parametric study

4.1 Multi-body interaction

To examine the influence of nonlinear multi-body interaction, we firstly consider a front-back array of OWSCs, each non-dimensional width B=3.15, mass m_a=0.49, I=0.42, thickness L=0.42, height h=1.52, mechanical stiffness b_{pto}=1.0 and mechanical damping c_{pto}=1.0 at water depth d=1.49. The gap between two OWSCs is S=9.49. The detail information of each OWSC model has been given in Section 3.1. Fig. 6(a)-(d) gives the motion amplitude γ^m, average energy $E^m{}_p$, individual interaction factor q^m_{ind} and capture efficiency R of each OWC in the array system with incident wave height H_I=0.18. The corresponding results of an isolated OWSC in open water is also presented in these figures. It can be seen that the total motion displacement of each OWSC in the array system initially increases with wave period, and arrives at the maximum at a critical T, then further decrease after that. The maximum displacement of front OWSC occurs at wave period T=9.9, and the displacement at period range 8<T<12 is larger than that of an isolated OWSC. This is because the gap between two OWSC is close to the wave length with T=9.1 ("s" has been deleted) according to the dispersion equation $\omega^2 = gk\tanh kd$, and under this condition, the incident wave and the reflected wave from the back OWSC are out of phase acting on the front OWSC ("in phase" has been revised as "out of phase") and induce strong horizontal wave force. However, when wave period exceeds this range, the wave interference is out of phase and the displacement is mitigated as compared with the counterpart with isolated OWSC. The individual interaction factor of front OWSC is larger than 1 within wave resonant region (8<T<12), which further indicates the constructive multi-body hydrodynamic interaction. Furthermore, the front OWSC creates a secondary higher energy extraction at 12<T<17. The secondary enhancement of energy extraction occurred when the mechanical damping b_{pto} is near the optimal damping b_{opt} with wave period T=16. For example, at wave period T=16, b_{opt} of the front OWSC is 1.15 based on Eq. (18), while b_{pto} is set as 1.0 in this case. Thus, a secondary peak of individual interaction factor occurs. In the particular case, due to the shield effect generated by front OWSC, the energy extraction of the back OWSC is always smaller than that of isolated OWSC, and thus design of back OWSC should be determined with rigorous analysis.

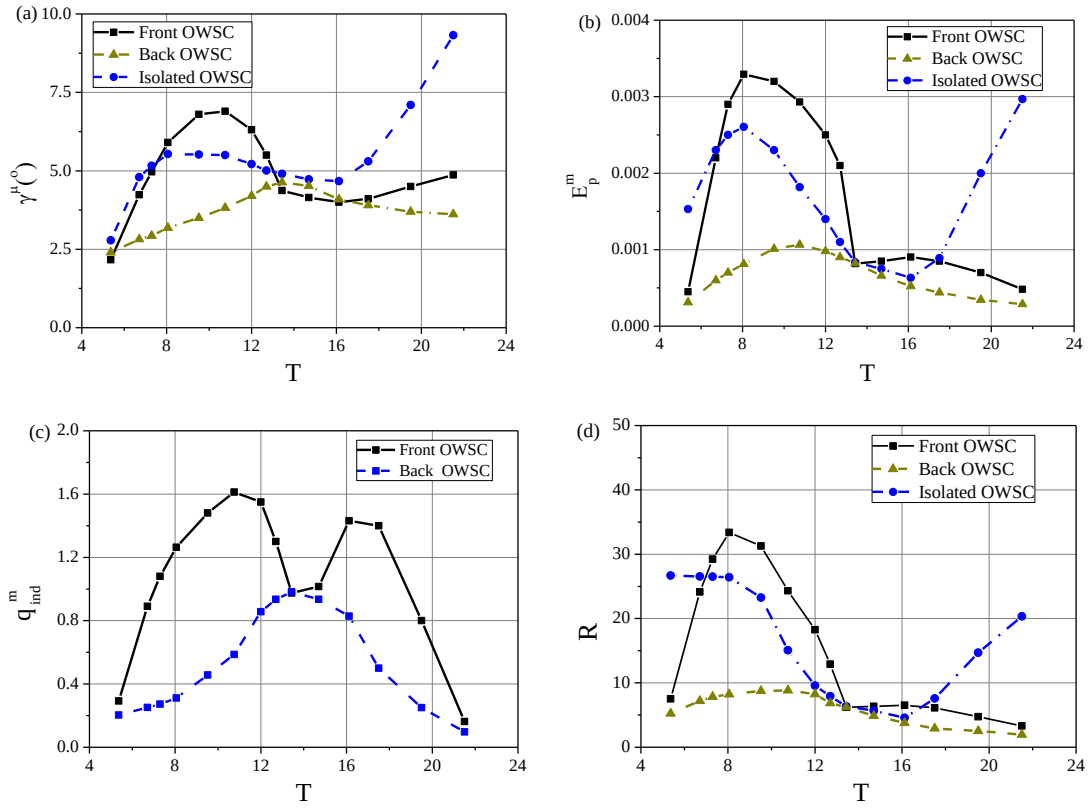

Fig. 6. Variations of (a) the motion amplitude γ^m, (b) average energy $E^m{}_p$, (c) individual interaction factor q^m_{ind} and (d) capture efficiency R versus wave period T for a front-back array system in comparison with those of an isolated OWSC device

4.2 Wave height effect

To illustrate the influence of wave height on the hydrodynamic performance of the front-back array of dual-OWSC, the numerical simulation is conducted with three different wave heights: H_I=0.18, 0.32 and 0.52 and the other parameters are kept ("fixed" has been revised as "kept") the same with those in Fig. 6. Fig. 7 shows the amplitude response operator (RAO) of each OWSC for different wave heights. It can be seen that the maximum response of front OWSC is larger than that of back OWSC, and the ("this" has been revised as "the") opposite is true for the resonant period due to the fluid push of the gap between two OWSCs. As wave height increases, motion response of the front OWSC decreases in high frequency region and vice versa in low frequency region. However, for the back OWSC device, the motion response in high frequency region decreases when wave height increases from 0.18 to 0.32, and then almost remain the same when wave height increases from 0.32 to 0.52. Conversely, in the low frequency region, the motion response of back OWSC first ("firstly" has been revised as "first") increases and then decreases with increasing wave height. The RAO peak of front OWSC occurs at H_I=0.18 among three wave heights and that of back OWSC occurs at H_I=0.32.

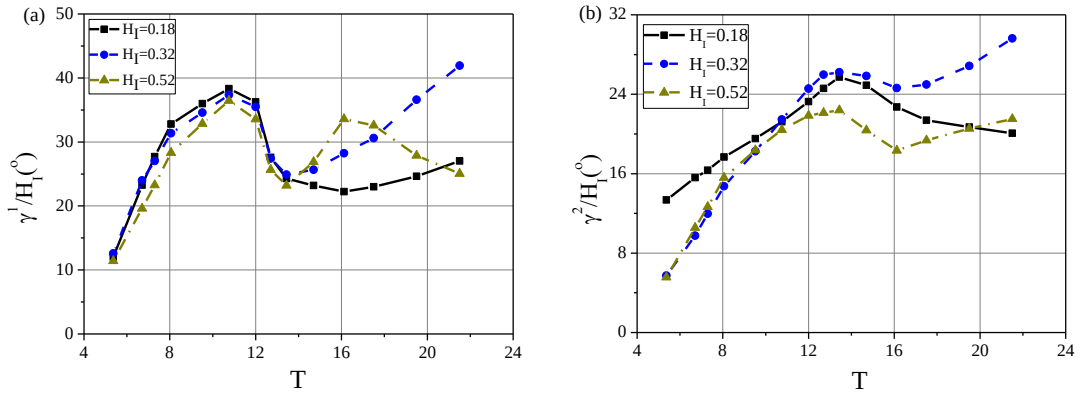

Fig. 7. Variations of the motion amplitude for (a) the front OWSC γ^1 and (b) the back OWSC γ^2 versus wave period T with different incident wave heights

According to wave theory, the wave energy is proportional to the square of H_I, and thus $E^{1/2}{}_p/H^2{}_I$ of each OWSC against wave period T with different wave heights H_I, is given in Fig. 8. It can be observed that in wave resonant region ($8<T<12$), the average energy of front OWSC decreases with increasing wave height, but follows a completely opposite variation in other wave period region. This indicates that the fluid motion ("violent wave" has been revised as "fluid") between two OWSCs can affect the wave energy extraction of OWSC device due to the irregular horizontal motion of water particle. On the other hand, the effect of wave height on wave energy extraction of the back OWSC device is more complicated. For example, when wave period is less than 14, the energy extraction firstly decreases and then increases with wave height, and the resonant period of OWSC first ("firstly" has been revised as "first") decreases and then stays ("keeps" has been revised as "stays") the same with wave height. This is because added mass of the back OWSC decrease to the minimum value when wave height increases from 0.18 to 0.32 and then is almost unchanged after that. The resonant period can be obtained as

$$T_n^m = \frac{2\pi}{\sqrt{\dfrac{c_{pto}^m + c_z^m}{I^m + a_z^m}}} \tag{24}$$

The added mass influences the ("is a determined factor to" has been revised as "influences the") resonant period, which can be clearly observed in Eq. (24). It is also interesting that double peak phenomenon appears ("is presented" has been revised as "appears") in the average energy of the back OWSC device with increasing wave height.

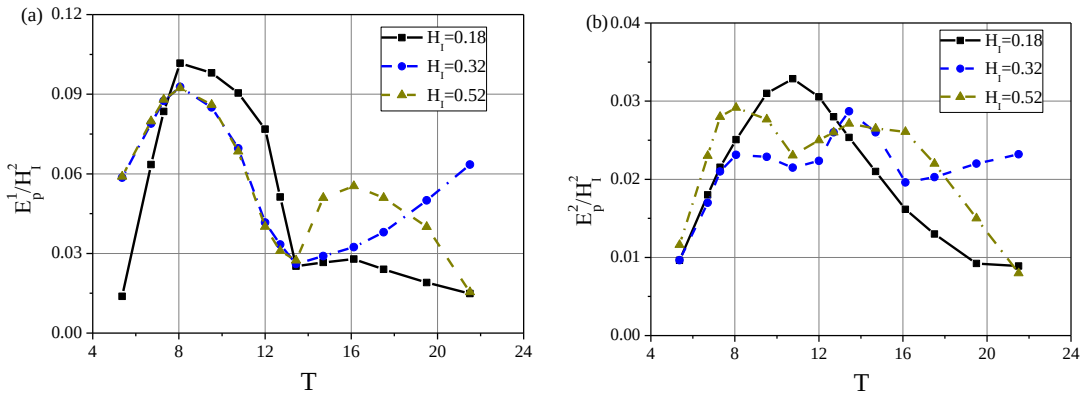

Fig. 8. Variations of the average generated power for (a) the front OWSC $E^1{}_p/H^2{}_I$ and (b) the back OWSC $E^2{}_p/H^2{}_I$

versus wave period T with different incident wave heights

Then the mean interaction factor q_{mean} and the total capture efficiency of the front-back array of OWSCs against wave period with different wave height is shown in Fig. 9. When wave height is larger than 0.32, the mean interaction factor always is smaller than 1 within whole tested period, which implies that the wave nonlinearity worsens the wave energy extraction performance of the array configuration compared to isolated OWSC device. For incident waves with small height i.e. H_I=0.18, the total average energy E_P at wave period T=10.5 and 16 are enhanced up to 1.15 and 1.18 times, respectively, as compared to the isolated OWSC. This may be because the decreasing rate of the wave energy extraction for single OWSC device is smaller than that for the front-back array of dual-OWSC system when the incident wave amplitude increases. In addition, when wave amplitude is small, the trend of the fluid motion in the gap between OWSCs with time is periodic and regular, which may lead to a constructive interference with incident waves. However, as wave amplitude increases, the trend of fluid motion are not regular and higher-order waves occur, which amplifies the adverse nonlinear effect. Therefore, the wave resonance in the gap between OWSCs has a beneficial effect on wave energy extraction for small wave amplitude and has an adverse effect for large wave amplitude. The capture efficiency R depicted in Fig. 9 (b) reveals that the capture efficiency R has an obvious reduction in wave resonant region ($8<T<14$) with increasing wave height and vice versa at larger or smaller wave period.

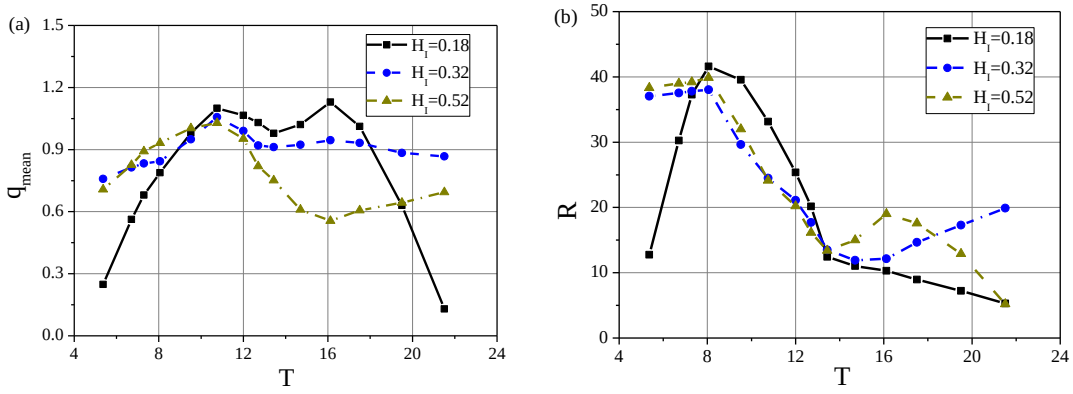

Fig. 9. Variations of (a) the mean interaction factor q_{mean} and (b) the capture efficiency R versus wave period T with different incident wave heights

4.3 Gap effect

The effect of the gap between front-back array OWSCs is investigated in this section with three cases of different gaps i.e. S=0.25λ, 0.5λ and 1.0λ where λ is incident wave length. In this set of numerical simulations, the incident wave height H_I=0.18 and other parameters are unchanged. Fig. 10 gives the variation of motion amplitude of each OWSC with wave period. From Fig. 10(a), it can be observed that for the case of S=0.25λ, ("When the gap is equal to 0.25λ," has been revised as "From Fig. 10(a), it can be observed that for the case of S=0.25λ,") the motion amplitude of front OWSC firstly increases to maximum with wave period and then decreases after that. However, for cases of S=0.5λ and 1.0λ, there are two peak values of motion amplitude near T=10.05 and T=16.10. ("but for S=0.5λ or 1.0λ, that oscillates between its peak and valley values." has been revised as "However, for cases of S=0.5λ and 1.0λ, there are two peak values of motion amplitude near T=10.05 and T=16.10.") This reason is due to that the motion amplitude of front OWSC is determined by both the resonant feature and the push effect of the back OWSC. When the gap is enough small, the shielding effect of front OWSC is obvious that leads to small interaction between front and back

OWSCs, and thus the maximum motion of front OWSC is almost dominated by the resonant period. As the gap increases, the shielding effect is gradually reduced and the fluid resonance in the gap leads to the second peak value of the motion amplitude. When the gap further increases to 1.00λ, the maximum motion induced by the internal fluid resonance is comparable with that induced by the structure resonance. The motion of the front OWSC for S=0.25λ is generally larger than that for S=0.5λ and S=1.0λ, particularly near the resonant period of the OWSC, but it follows an opposite trend for the back OWSC in Fig. 10(b). Overall, the motion amplitude of the front OWSC in Fig. 10(a) is more sensitive to the change of the gap compared with that of the back OWSC in Fig. 10(b).

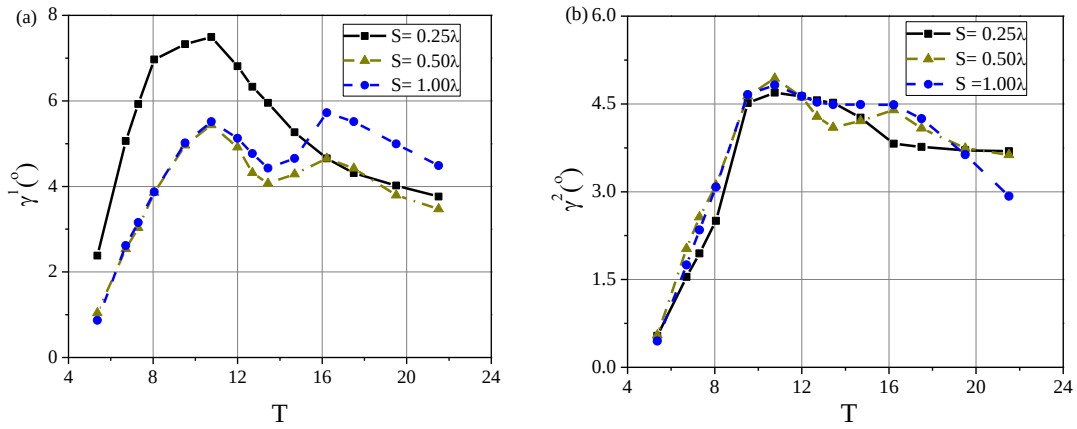

Fig. 10. Variations of the motion amplitude for (a) the front OWSC γ^1 and (b) the back OWSC γ^2 versus wave period T with different gap distances between OWSCs

For an array of OWSC system, the shielding effect of the front OWSC device changes the exciting force acting the back one, and the forth-back oscillation of each OWSC device exerts a radiation force on the adjacent OWCS device. Fig. 11 shows the non-dimensional amplitude of the horizontal wave force F_x^m of each OWSC device as the function of both wave period and gap. It can be observed that for each OWSC device, the variation trend of horizontal wave force with gap is almost identical with that of rotational displacement in Fig. 10. This is because that the OWSC device mainly converts wave energy from the horizontal movement of the water particles in waves which can be enhanced in the shallow water region due to shoaling effect, and its wave force in Eq. (5) mainly depends on the horizontal component. Additionally, the wave force acting on the back OWSC device in Fig. 11(b) at each frequency is smaller than that acting the front one in Fig. 11(a). This is due to two important factors. First, the shielding effect generated by the front OWSC device reduces the wave loads on the back one, especially in short wave region. Second, the motion of the front OWSC device captures some of wave energy in the flow field, which leads to smaller transmission wave force.

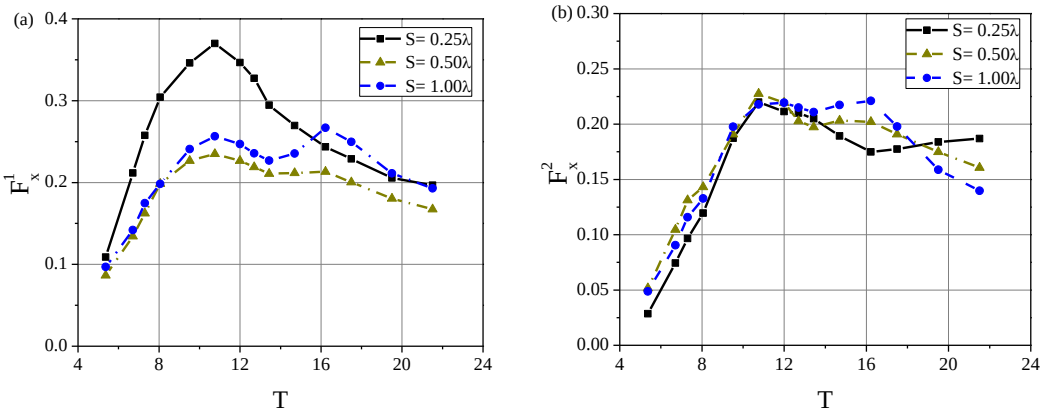

Fig. 11. Variations of the horizontal wave force for (a) the front OWSC F_x^1 and (b) the back OWSC F_x^2 versus wave period T with different gap distances between OWSCs

Fig. 12 gives the average energy of the dual array OWSCs for different gaps. The maximum average energy at S=0.25λ is larger than that at S=0.50λ and S=1.00λ, which occurs at resonant period T=8 and 10 for the front OWSC in Fig. 12(a) and the back OWSC in Fig. 12(b), respectively. At smaller periods, the average energy of the front OWSC is the maximum value among these three gaps and vice versa for the back OWSC due to energy exchange. However, at lager periods, the average energy of the front OWSC increases with increasing the gap. When the gap increases from S=0.50λ to S=1.00λ, the average energy of the back OWSC has a sudden reduction at period T=21.9, which can be attributed to the increase of the fluid mass in the gap. Because the relative gap S/λ is the determining factor in the wave resonance in large-period long wave region, and the gap between OWSCs is large enough for S/λ=1.00 at T=21.9 such that the increases of the internal fluid mass in the gap mitigate the internal fluid motion.

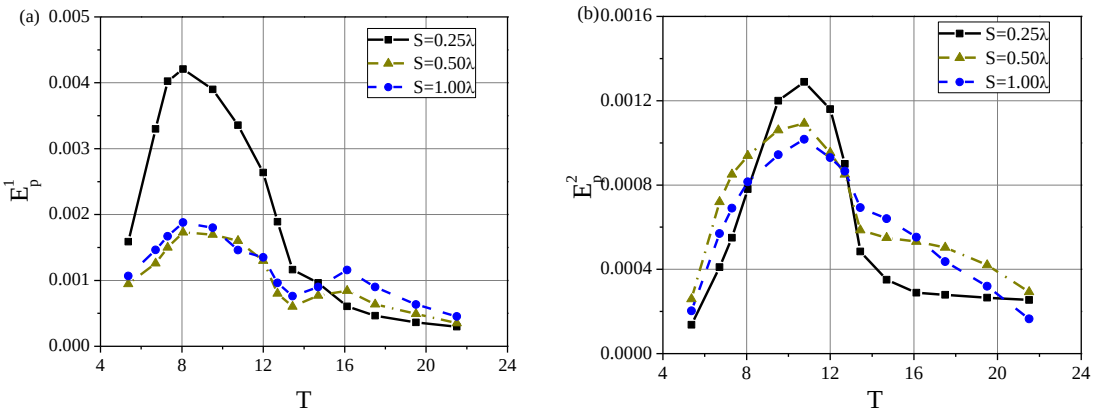

Fig. 12. Variations of the average generated power for (a) the front OWSC E^1_p/H^2_I and (b) the back OWSC E^2_p/H^2_I versus wave period T with different gap distances between OWSCs

Fig. 13 (a)-(d) gives the variations of the individual interaction factor q_{ind}^m, the mean interaction factor q_{mean} and the total capture efficiency R with wave period for different gaps. When the gap is enough smaller i.e. S=0.25λ, the individual interaction factor q_{ind}^1 of the front OWSC in short wave region (T<14) is always larger than 1, as shown in Fig. 13(a), implying the constructive effect of multi-body hydrodynamic interaction. When the gap is larger than 0.5λ, the wave resonance in the gap at T=16 make the front OWSC keep higher energy extraction than isolated OWSC device, while the lower energy extraction of the back OWSC is due to the shielding effect of the front OWSC, as shown in Fig. 13(b). The total mean interaction factor q_{mean} shown in Fig. 13(c) reveals that the smaller gap in short wave region and the larger gap in long wave region have constructive effects

on the energy extraction of the OWSC device, respectively. This conclusion indicates that, for practical engineering applications, the configuration of the multi-group front-back array of OWSCs with different gaps will be more advisable, since higher energy extraction can be realized over whole wave period range in irregular waves. The capture efficiency R shown in Fig. 13 (d) increases with decreasing gap in short wave region, but it follows a completely opposite trend in the long wave region. This can be explained by the fluid mass and the fluid velocity in the gap. The momentum of water particle in the gap is proportional to the fluid mass and velocity. In short wave region, the smaller gap induces stronger ("more violent" has been revised as "stronger") wave resonance in the gap due to smaller fluid mass. In contrast, in the long wave region, the incident wave includes higher energy which can induce wave resonance with larger fluid mass, so the larger gap leads to larger wave momentum in the gap.

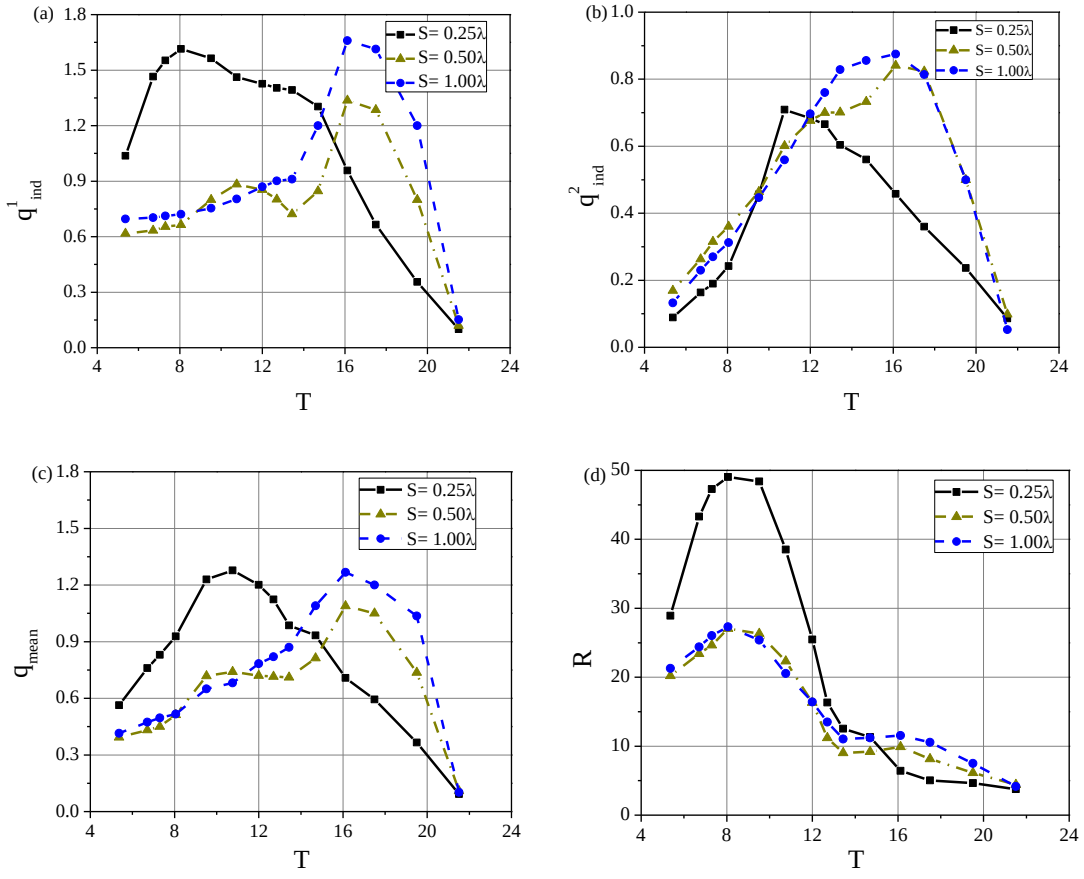

Fig. 13. Variations of (a) the individual interaction factor for the front OWSC q^1_{ind}, (b) the individual interaction factor for the back OWSC q^2_{ind}, (c) the mean interaction factor q_{mean} and (d) the capture efficiency R versus wave period T with different gap distances between OWSCs

4.4 PTO effect

As indicated in Eqs. (4), (12) and (20), the PTO coefficients have significant effect on the motion response, extracted energy and capture efficiency of an array of OWSCs, which could be an important factor in OWSC design and analysis. Keeping the parameters S=9.49, H_I=0.18, T=12, Fig. 14-16 gives the effects of the PTO stiffness coefficient c_{pto} and the PTO damping coefficient b_{pto} on the motion amplitude γ^m, average energy E^m_p, and capture efficiency R of each OWC in the array system. It can be seen from Fig. 14(a) and (b) that the motions of both front and back OWSCs decrease with increasing c_{pto} or b_{pto} due to additional restoring force or damping force expressed in

Eq. (4). However, the average energy of each OWSC initially increases with increasing PTO damping, and reaches the peak value at an optimal damping, then decreases as PTO damping further increases. Such behavior can be explained by Eqs. (4) and (12). The rotational speed of the OWSC device is inversely proportional to the PTO damping, while the extracted energy is proportional to both the PTO damping and square of flap speed. This indicated that the optimal damping formulized in Eq. (18) is a determining factor in energy extraction. In addition, the optimal damping increases with increasing PTO stiffness as shown in Fig. 15, and for fixed PTO stiffness, the optimal damping of each OWSC is different due to fluid motion in the gap between OWSCs. For example, for the front OWSC device, the optimal damping occurs at b_{pto} =0.4 (c_{pto}=0.50), 0.6 (c_{pto}=0.75) and 1.0 (c_{pto}=1.00). For the back OWSC device, the optimal damping occurs at b_{pto} =0.8 (c_{pto}=0.50), 1.0 (c_{pto}=0.75) and 1.2 (c_{pto}=1.00). Fig. 16 reveals that the capture efficiency of the array of OWSC device increases with decreasing PTO stiffness, and reaches the maximum with R=60% (c_{pto}=0.50), 43% (c_{pto}=0.75) and 33% (c_{pto}=1.00) at the optimal damping of the front OWSC.

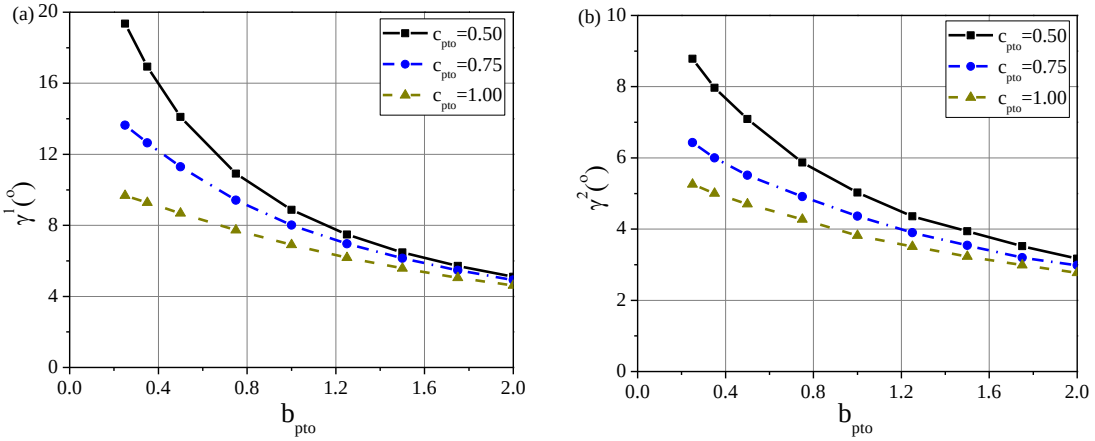

Fig. 14. Variations of the motion amplitude for (a) the front OWSC γ^1 and (b) the back OWSC γ^2 against different PTO damping coefficients b_{pto} and stiffness coefficients c_{pto}

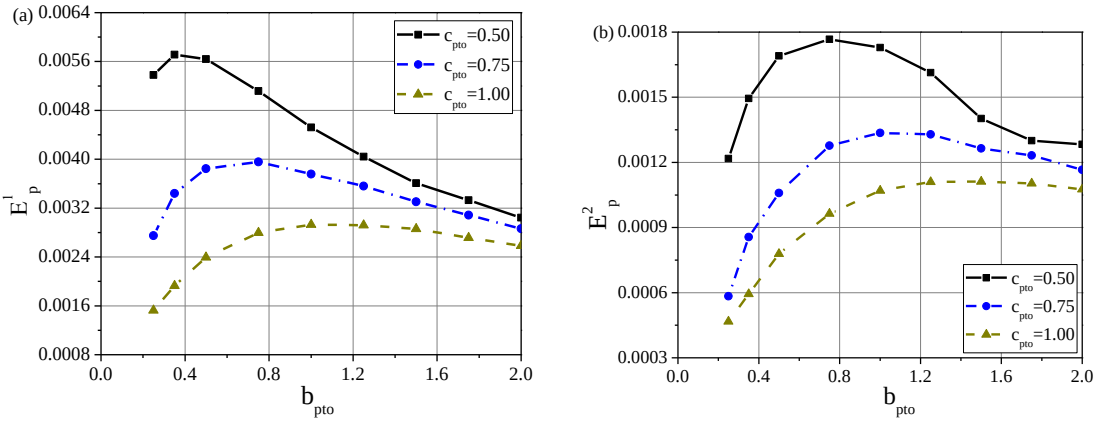

Fig. 15. Variations of the average generated power for (a) the front OWSC E^1_p/H^2_I and (b) the back OWSC E^2_p/H^2_I against different PTO damping coefficients b_{pto} and stiffness coefficients c_{pto}

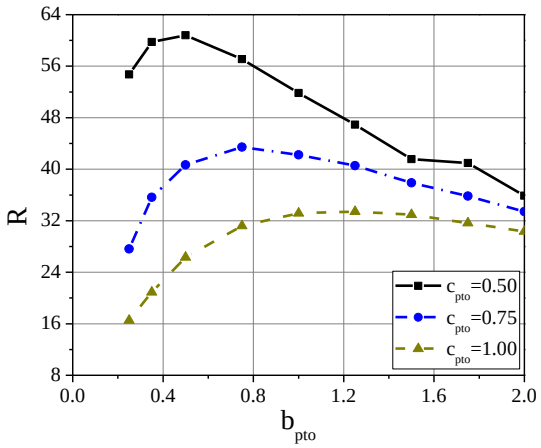

Fig. 16. Variations of the capture efficiency against different PTO damping coefficients b_{pto} and stiffness coefficients c_{pto}

4.5 Layout effect

So far, the developed numerical model has been used to investigate the hydrodynamic performance of two identical front-back OWSCs only. Furthermore, what will happen if the number of OWSCs is kept the same, while the different layout schemes are considered. To answer above question, numerical model has been applied with three types of layout, as show in Fig. 17 (in-line array configuration, front-back array configuration and staggered array configuration). The simulated results are shown in Figs. 17-19 at S=2.098, H_I=0.18, b_{pto}=0.35 and c_{pto}=0.5. Fig. 18 gives the variation of motion amplitude γ^m of each OWSC with wave period for different layouts. It can be seen that two identical in-line OWSCs oscillate at unison due to perpendicular incident wave to the flap width and the layout symmetry. The rotational angle of the front OWSC is larger for a front-back or staggered layout than that for an in-line layout due to the motion of internal fluid in the gap, as shown in Fig. 18(a). In addition, the resonant response of the front OWSC for a staggered layout is largest among three different layouts. This means that the back OWSC is partly shielded to cause stronger motion of the front OWSC. However, the resonant response of the back OWSC for an in-line layout is largest because of completely facing waves, as shown in Fig. 18(b). The resonant responses for different layouts correspond to almost the same wave period, which implies that the resonant frequency in this small gap case is not very sensitive to the change of layout scheme.

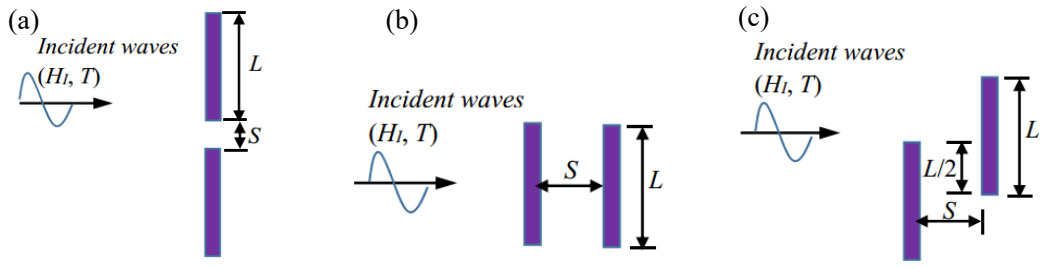

Fig. 17. Configuration of (a) an in-line array system, (b) a front-back array system and (c) a staggered array system

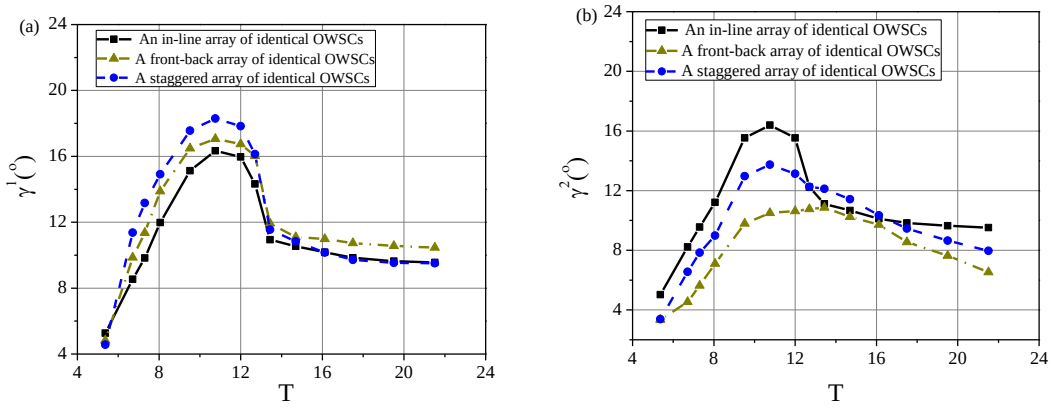

Fig. 18. Variations of the motion amplitude for (a) the front OWSC γ^1 and (b) the back OWSC γ^2 versus wave period T with different array layouts

Fig. 19 gives the variation of average energy $E^m{}_p$ of each OWSC with wave period for different layouts. As shown in Fig. 19 (a), the wave energy extraction of the front OWSC for a staggered layout is largest near the resonant period, which is identical with the motion curve depicted in Fig. 18 (a). Fig. 19 (b) also reveals that the energy extraction of the OWSC for an in-line layout is larger than that of the back OWSC for both front-back and staggered layouts at almost whole tested range of wave period. The average energy of the OWSC for an in-line layout suddenly decreases when wave period increase from T=11 to 13, but that of the back OWSC for a staggered layout decease tenderly, which leads to that the energy extraction of the back OWSC for a staggered layout is higher than that for an in-line layout at certain periods i.e. T=13 ("at T=13" has been revised as "at certain periods i.e. T=13"). This is because the multi-body interaction in a staggered layout is stronger than that in an in-line layout, and OWSCs in the in-line layout need to be closer to each other than those in the staggered layout in order to interfere constructively. In addition, the optimal PTO damping could be varied among different array layouts, making it possible to increase wave energy extraction for a staggered layout compared with that for an in-line layout for a fixed wave period. ("This is because the two OWSCs for in-line layout orient completely the waves, and the variation of the pressure difference on the two sides of the OWSCs are more pronounced than that for a staggered layout due to the shielding effect." has been revised as "This is because the multi-body interaction in a staggered layout is stronger than that in an in-line layout, and OWSCs in the in-line layout need to be closer to each other than those in the staggered layout in order to interfere constructively. In addition, the optimal PTO damping could be varied among different array layouts, making it possible to increase wave energy extraction for a staggered layout compared with that for an in-line layout for a fixed wave period.")

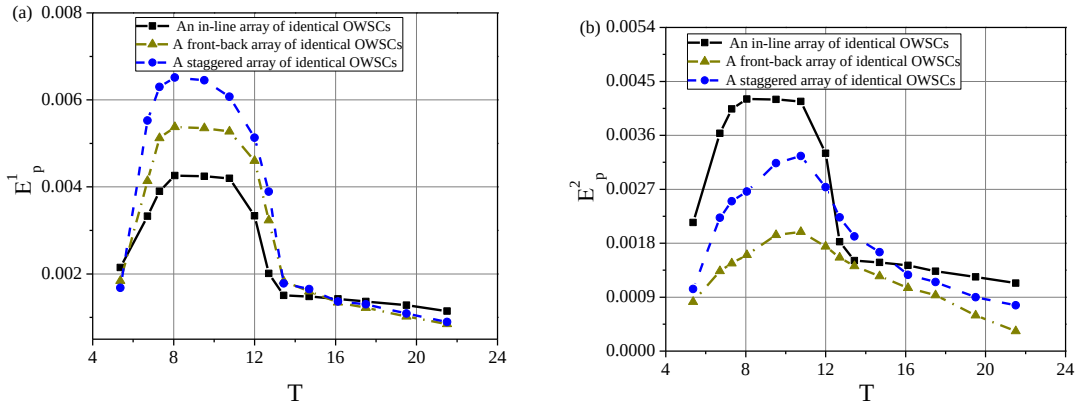

Fig. 19. Variations of the average generated power for (a) the front OWSC E^1_p/H^2_I and (b) the back OWSC E^2_p/H^2_I versus wave period T with different array layouts

Fig. 20(a)-(c) gives the individual interaction factor q^m_{ind} and the mean interaction factor q_{mean} as the function of both wave period and layout. From Fig. 20(a) and (b), it can be seen that the wave effect between sides of the OWSCs is constructive for an in-line layout in short wave region (T<12), but that can be ignored in long wave region (T>12), which is because a large pressure difference can be generated between the sides of the OWSCs in short waves, but pressure field is insensitive to variation of long wave period. Near the resonant period, the individual interaction factor of the front OWSC for a front-back layout and a staggered layout is larger than that for an inline layout, revealing the benefit effect of the fluid motion in gap between OWSCs. However, the individual interaction factor of the front OWSC for a front-back layout and a staggered layout is smaller than 1, which indicates that the small gap can worsen the energy extraction of the back OWSC. As shown in Fig. 20(c), the total mean interaction factor near resonant period (8<T<16) for a staggered layout is larger than that for other two layouts, but that in shorter waves (T<8) or longer waves (T>16) is largest for an in-line layout. This further implies that the combination of the in-line layout and the staggered layout i.e. triple-array configuration would be preferable selection due to higher wave energy extraction and should be rigorously analysed with parametric simulations in a further work.

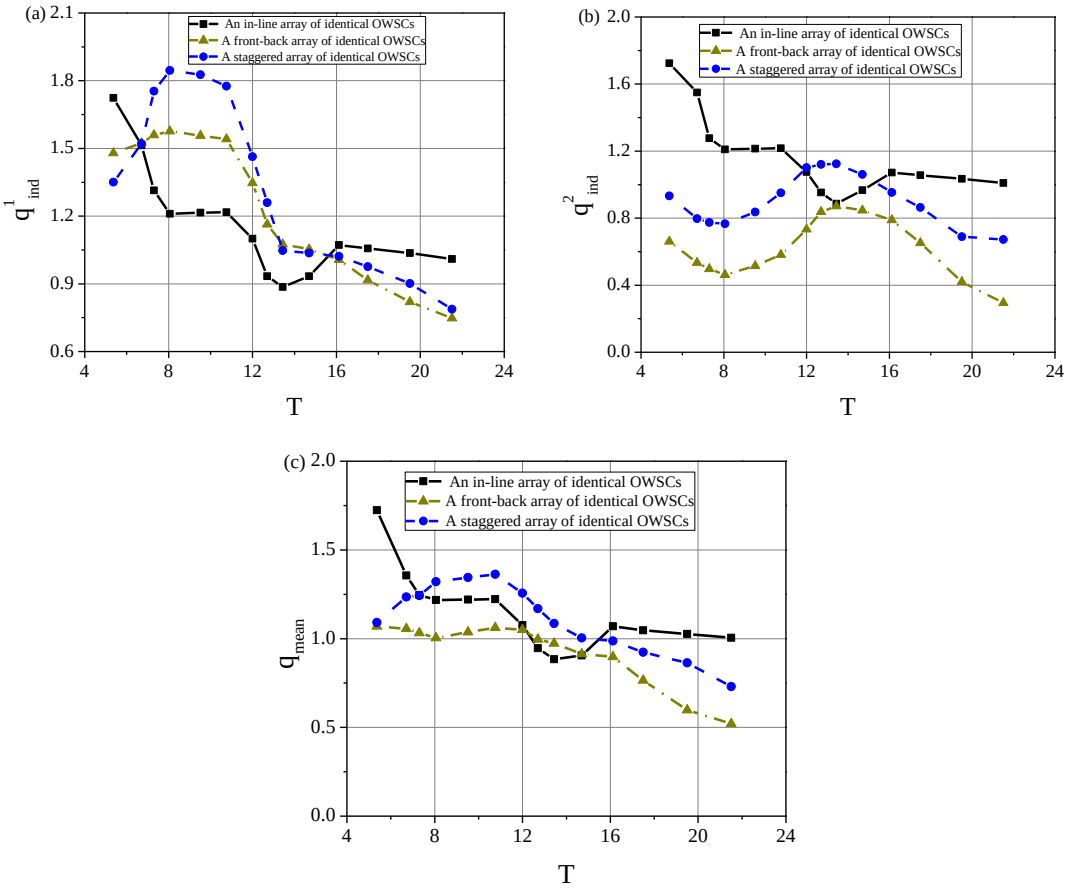

Fig. 20. Variations of (a) the individual interaction factor for the front OWSC q^1_{ind}, (b) the individual interaction factor for the back OWSC q^2_{ind}, and (c) the mean interaction factor q_{mean} versus wave period T with different array layouts

The capture efficiency R of wave energy is shown in Fig. 21. The variation trends in Fig. 21 (a) and (b) are similar for three different layouts. The peak efficiency of the front OWSC near resonant

period for three layouts can reach 43% (an in-line array), 54% (a front-back array) and 67% (a staggered array), respectively. This efficiency enhancement for a staggered array is caused by the amplified coupling effect of the fluid motion between flap sides and front-back flaps. The capture efficiency of the back OWSC for a front-back array layout is obviously lower than that for an in-line array layout in short wave region (T<12), but the difference in long wave region (T>12) is gradually reduced. A reason to such a phenomenon is that in short wave region, the gap between front and back OWSCs is not small relative to wavelength, son that the shielding effect of front OWSC is obvious. In contrast, in long wave region, the gap is enough small compared to wavelength, implying that the incident wave can almost transmit over the front OWSC and interact with the back OWSC, so that the gap effect is insensitive to the increase of long wave length.

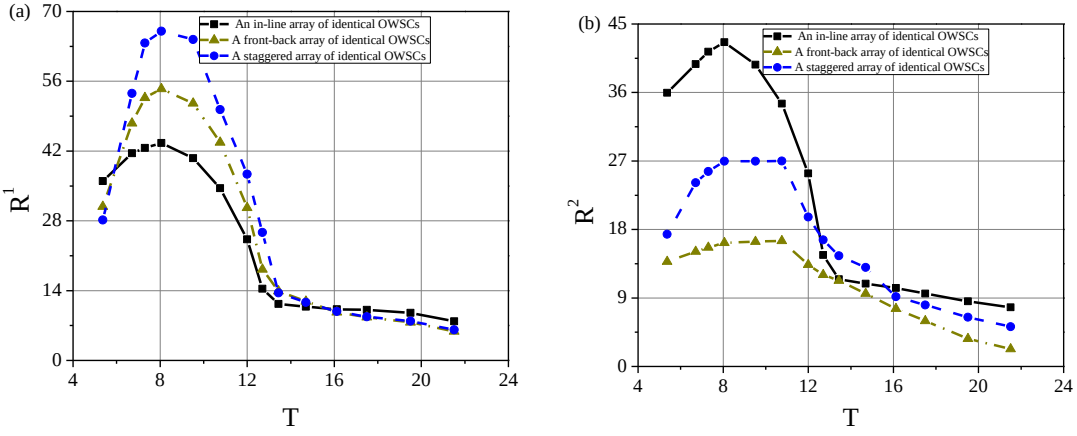

Fig. 21. Variations of the capture efficiency for (a) the front OWSC R^1 and (b) the back OWSC R^2 versus wave period T with different array layouts

4.6 Wave direction effect

Since the incident wave direction is random in realistic ocean environment, the energy extraction of the array OWSC devices for arbitrary wave incident direction is also examined numerically. Fig. 22 shows the contour of wave surface elevation when a wave crest propagates at the front OWSC for three different layouts described in above section and three different incident wave angles i.e. θ=0°, 15° and 30°. Here, the wave period and wave height are T=5 and H_I=0.18, respectively. It can be seen from Fig. 22 (a)-(c) that, for incident wave angle θ=0°, an in-line array system generates stronger disturbance of wave surface around each OWSC compared to other array layouts ("than" has been revised as "compared to" and "front OWSC of" has been revised), which leads to a larger fluid pressure difference between left and right sides of each OWSC. Hence, an in-line array system experiences a lager back and forth oscillating motion. In addition, due to shielding effect, the difference of wave surface (and also fluid pressure) around back OWSC for a staggered array system and a front- back array system is significantly smaller than that for an in-line array system. As incident wave angle increases, an in-line array system undergoes more elevation jumps of wave surface as shown in Fig. 22 (d) and (g), and the fluid filed becomes more complex. The asymmetry of wave surface around the ("relative to" has been revised as "around the") array layout makes both two OWSCs impossible to subjected to impingement of wave crest simultaneously. Accordingly, when the front OWSC experiences a crest jump in wave surface or pressure between its both sides, the back OWSC would be surrounded by a wave trough which causes smaller rotational force moment. The wave surface in the gap between OWSC for a staggered array system undergo stronger motion with increasing incident wave angle, which is because the effect wave length in the direction

normal to flap width is gradually close to the gap value as incident wave angle increases. As a consequence, the front OWSC in waves with large incident angle i.e. θ=30º, would be subjected to wave crest and trough action at the same time as shown in Fig. 22 (h). It is also clear in Fig. 22 (f) and (i) that for a front-back array system, the fluid motion in the gap between OWSCs is further strengthened with increasing incident wave angle ("becomes more pronounced" has been revised "is further strengthened"), where the reflected zone situated at the weather side of the front OWSC is expanding, while the back OWSC undergoes a jump in wave surface (fluid pressure). This leads to a wave crest interaction with both front and back OWSCs simultaneously. If allowed to oscillate, both OWSCs would rotate toward the right induced by a clockwise fluid force moment.

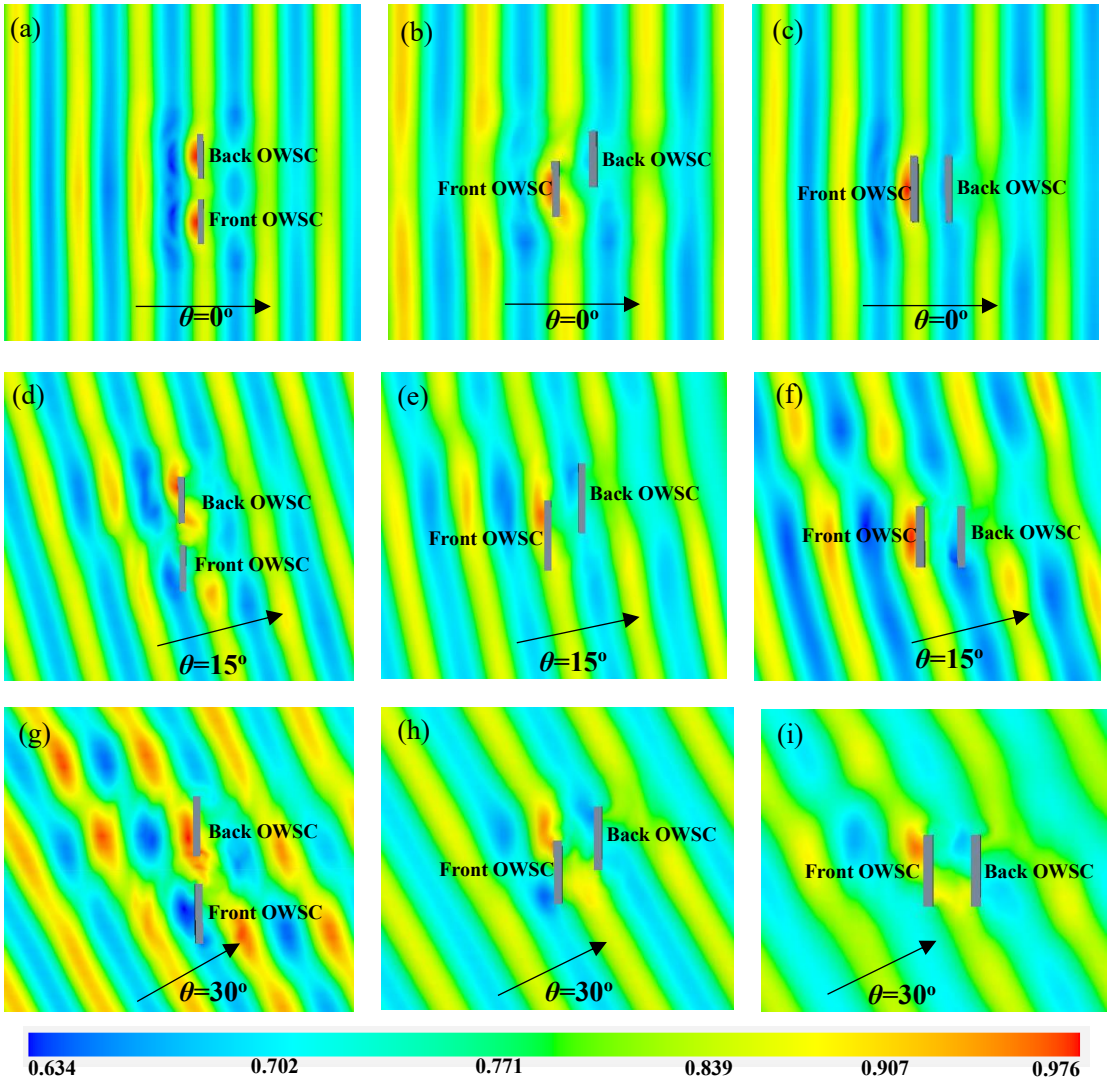

Fig. 22. 3D contour map of the total free surface when an oblique wave crest meets the front OWSC for different array layouts and incident wave angles i.e. (a) an in-line array subjected wave action with θ=0º, (b) a staggered array subjected wave action with θ=0º, (c) a front-back array subjected wave action with θ=0º, (d) an in-line array subjected wave action with θ=15º, (e) a staggered array subjected wave action with θ=15º, (f) a front-back array subjected wave action with θ=15º, (a) an in-line array subjected wave action with θ=30º, (b) a staggered array subjected wave action with θ=30º and (c) a front-back array subjected wave action with θ=30º

Fig. 23 shows the variation of the motion amplitude of each OWSC device with incident wave angle θ for different layouts. From Fig. 23(a), it can be observed that when all array OWSC devices

are subjected oblique wave action, the motion amplitude of front OWSC for a front-back array layout is larger than that for an in-line array and a staggered array. For a staggered array, the motion amplitude of front OWSC firstly decreases as incident wave angle increases from 0° to 30°, and then increases after that. The turning point for an in-line array shifts to larger incident wave angle i.e. θ=60°. This is due to multi-body interaction for an in-line array only including both sides of two OWSC devices. When incident wave angle is smaller than 30°, the motion amplitude of back OWSC for an in-line array is obviously larger than that for other two layouts, and that for a front-back array is minimum as shown in Fig. 23(b). However, as incident wave angle continues to increase, the motion amplitude of back OWSC for a front-back array is maximum. This is because that the shielding effect on the motion of back OWSC is more dominant than the multi-body interaction for smaller incident angle, but this opposite is true for larger incident angle. Overall, the total motion amplitudes of front OWSC for an in-line array and a staggered array rapidly decrease with increasing incident wave angle, while that for a front-back array layout slightly decreases with incident wave angle. This indicates that the motion responses for an in-line array and a staggered array are more sensitive to incident angle than that for a front-back array.

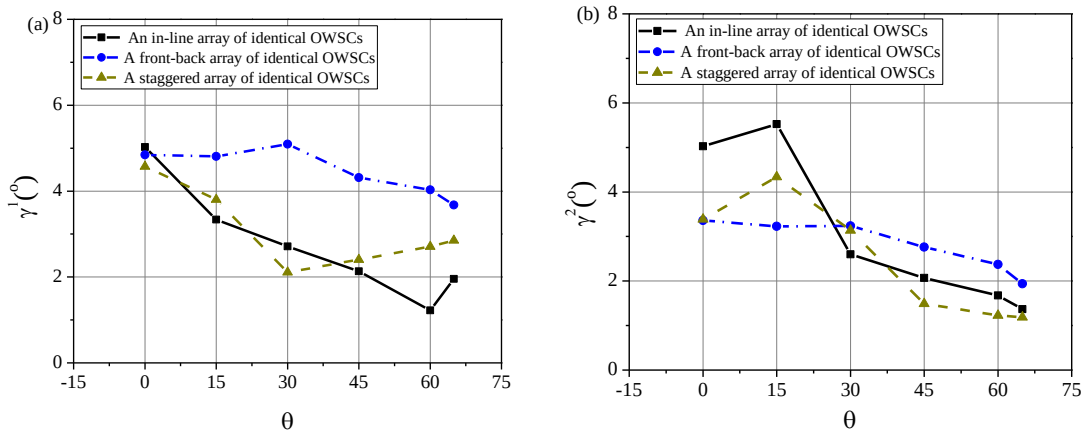

Fig. 23. Variations of the motion amplitude for (a) the front OWSC γ^1 and (b) the back OWSC γ^2 versus incident wave angle θ with different array layouts

Fig. 24 gives the distribution of average energy E^m_p of each OWSC for different layouts. It is shown that the wave energy extraction of front OWSC increases with increasing incident wave angle for all layouts, as shown in Fig. 24(a). This is due to the reduction of effective wavelength perpendicular to flap width. It should be noted that the energy extraction of the back OWSC for an in-line array and a staggered array has an increased trend when oblique wave incident angle is smaller than 15°, as shown in Fig. 24(b). This is because of the fact that the wave surface disturbance is gradually generated between the sides of two OWSCs as incident wave angle increases. Hence, this also implies that for practical applications, an array of OWSC with different relative distance between sides would be more advisable, since the realistic waves involves multi-direction and multi-frequency component.

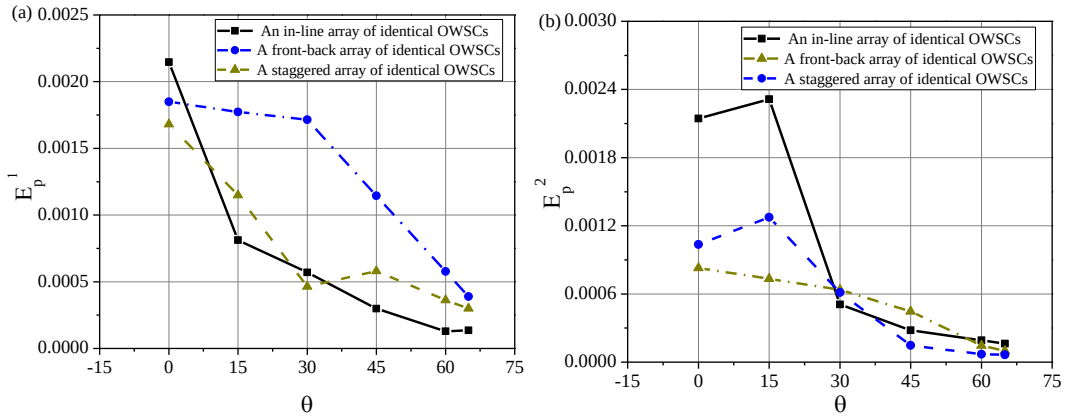

Fig. 24. Variations of the average generated power for (a) the front OWSC E^1_p/H^2_I and (b) the back OWSC E^2_p/H^2 versus incident wave angle θ with different array layouts

5 Conclusions

In this paper, a three-dimensional (3-D) ("3D" has been revised as "three-dimensional (3-D)") fully nonlinear potential flow theory in time domain is presented to study hydrodynamic characteristics of an array of dual-oscillating wave surge converter (OWSC) ("OWSC" has been revised as "dual-oscillating wave surge converter (OWSC)") system, focusing on the motion response, the average generated power, the mean interaction factor, the individual interaction factor and the energy capture efficiency. The time domain approach can be applied for the optimized configuration of wave energy converters, because it can accurately predict the coupled dynamic interaction of waves and this array system. The following significant and useful conclusions can be obtained from the presented results:

(1) For a front-back array of OWSC system, wave resonance in the gap between OWSCs enhances the energy extraction of OWSC devices, especially for the front OWSC device. The capture efficiency of the back OWSC device is lower than that of an isolated OWSC device due to shielding effect induced by the front OWSC device.

(2) With increasing incident wave height, both the average generated power and the capture efficiency of the front-back array of OWSC device near wave resonant region in the gap. This indicates that the strong wave nonlinearity effect has an adverse effect on wave energy extraction. In addition, the incident wave height has a more complex effect on the back OWSC than that on the front OWSC due to reduction of added mass with wave height.

(3) Narrower gap between OWSCs for a front-back array configuration, leads to a larger rotational motion of front OWSC device in small wave periods, and this is contrary to the motion of back OWSC device. As the gap distance increases, the wave energy extraction in large wave periods can be enhanced due to the wave resonance in the gap. Thus, for realistic irregular waves, the configuration of the multi-group front-back array of OWSC with different gap distances would be more feasible due to realization of multi-frequency wave resonance.

(4) Compared to an isolated OWSC device, an in-line array of dual-OWSC system can enhance wave energy extraction in small wave periods due to wave interaction between flap sides, while a staggered layout can extract more wave energy near wave resonance region. Therefore, multi-triple-array configuration would be a preferable selection for realistic wave farm because it broadens the effective bandwidth of energy extraction.

(5) When oblique waves interact with different layouts, the weather side of an in-line array system would be subjected to wave crest and trough loads simultaneously, leading to more jumps of wave surface around structures. However, the gap in a front-back array system and a staggered array system would experience more intense wave motion. (“, while” has been revised “. However,”) The total wave energy extraction decreases for all array layouts with increasing incident wave headings due to the reduction of effective wavelength perpendicular to flap width; meanwhile, the back OWSC in an in-line array and a staggered extract higher wave energy since incident wave heading is less than 15°, which is because of strong wave disturbance between flap sides.

The present numerical approach can be extended straightforwardly to arbitrary configuration of array OWSCs. If multi-OWSC system in realistic wave environment is considered, similar solution steps are employed to obtain accurately optimum configuration and PTO coefficients. The simulated results in this paper can provide a guideline to help in the parametric optimization, layout selection and durability analysis.

CRediT authorship contribution statement

Yong Cheng: Methodology, Software, Data curation, Writing-original draft, Supervision. **Chen Xi:** Validation, Formal analysis, Writing-original draft, Investigation. **Saishuai Dai:** Formal analysis, Data curation, Writing-review & editing, Supervision. **Chunyan Ji:** Writing-review & editing, Supervision. **Margot Cocard:** Writing-review & editing.

Declaration of Competing Interest

The authors declare that they have no known competing financial interests or personal relationships that could have appeared to influence the work reported in this paper.

Acknowledgement

The authors are grateful to the National Natural Science Foundation of China (Grant No. 51861130358, 51609109), the State Key Laboratory of Ocean Engineering, China (Shanghai Jiao Tong University) (Grant No. 1905) and the Newton Advanced Fellowships of the Royal Society.

Appendix A. Average generated power of an OWSC device

Considering the series expansion of angular displacement γ of each OWSC device in Section 2.3, the angular velocity of an OWSC device can be written as

$$\dot{\gamma} = \mathrm{Re}\left(\sum_{n=0}^{\infty} in\omega\gamma_n e^{in\omega t}\right) \tag{A.1}$$

Then, substituting Eq. (A.1) into (10), we have

$$E_p = \frac{b_{\mathrm{pto}}}{lT}\int_{t}^{t+lT} \mathrm{Re}\left(\sum_{n=0}^{\infty} in\omega\gamma_n e^{in\omega t}\right)^2 dt \tag{A.2}$$

According to the following orthogonal characteristic

$$\int_{t}^{t+iT} e^{in\omega t} e^{is\omega t} dt = 0 \qquad (n \neq s) \tag{A.3}$$

Eq. (A.2) can be expressed as

$$E_p = \frac{b_{\text{pto}}}{lT} \int_t^{t+lT} \sum_{n=0}^{\infty} n^2 \omega^2 \left|\gamma_n\right|^2 \text{Re}(e^{in\omega t})^2 \, dt \tag{A.4}$$

The exponential integration in Eq. (A. 4) can be written as

$$\int_t^{t+lT} \text{Re}(e^{in\omega t})^2 \, dt = \text{Re}\left\{ \int_t^{t+lT} \left[\sin(nwt) + \cos(nwt)\right]^2 \, dt \right\} = \frac{1}{2} lT \tag{A.5}$$

Substituting Eq. (A.5) into (A.4), the final expression of E_p can be given as follows

$$E_p = \frac{1}{2} b_{pto} \omega^2 \sum_{n=1}^{\infty} (n\left|\gamma_n\right|)^2 \tag{A.6}$$

References

[1] Esteban M, Leary D. Current developments and future prospects of offshore wind and ocean energy. Appl Energy 2012; 90: 128-136.

[2] Whittaker BT, Folley M. Nearshore oscillating wave surge converters and the development of Oyster. Phil Trans R Soc A 2012; 370: 345-364.

[3] Aquamarine Power Ltd. 2010 Oyster. See http://www.aquamarinepower.com.

[4] Sarkar D, Renzi E, Dias F. Wave farm modelling of oscillating wave surge converters. In: Proceedings of the Royal Society of London a: Mathematical, Physical and Engineering Sciences. The Royal Society, 2014.

[5] Noad IF, Porter R. Optimisation of arrays of flap-type oscillating wave surge converters. Appl Ocean Res 2015; 50: 237-253.

[6] Renzi E, Dias F. Relations for a periodic array of flap-type wave energy converters. Appl Ocean Res 2013; 39: 31-39.

[7] Renzi E, Abdolali A, Bellotti G, Dias F. Wave-power absorption from a finite array of oscillating wave surge converters. Renew Energy 2014; 63: 55-68.

[8] Greenwood C, Christie D, Venugopal V, Morrison J, Vogler A. Modelling performance of a small array of wave energy converters: comparison of Spectral and Boussinesq models. Energy, 2016; 113: 258-266.

[9] Sarkar D, Contal E, Vayatis N, Dias F. Prediction and optimization of wave energy converter arrays using a machine learning approach. Renew Energy 2016; 97: 504-517.

[10] Liu Z, Wang Y, Hua X. Proposal of a novel analytical wake model and array optimization of oscillating wave surge converter using differential evolution algorithm. Ocean Eng 2021; 219: 108380.

[11] Nguten HP, Wang CM, Luong VH. Two-mode WEC-type attachment for wave energy extraction and reduction of hydroelastic response of pontoon-type VLFS. Ocean Eng 2020; 197: 106875.

[12] Tay ZY, Venugopal V. Hydrodynamic interactions of oscillating wave surge converters in an array under random sea state. Ocean Eng 2017; 145: 382-394.

[13] Wei YJ, Rafiee A, Henry A, Dias F. Wave interaction with an oscillating wave surge converter, Part I: Viscous effects, Ocean Eng 2015; 104:185-203.

[14] Henry A, Kimmoun O, Nicholson J, Dupont G, Wei Y, Dias F. A two dimensional experimental investigation of slamming of an oscillating wave surge converter. In: Proceedings of the 24th International Offshore and Polar Engineering Conference, Busan, Korea, 2014, June, PP. 296-305.

[15] Brito M, Canelas RB, García-Feal O, Domínguez JM, Crespo AJC, Ferreira RML, Neves MG,

Teixeira L. A numerical tool for modelling oscillating wave surge converter with nonlinear mechanical constraints. Renew Energy 2020; 146: 2024-2043.
[16] Mottahedi HR, Anbarsooz M, Passandideh-Fard M. Application of a fictitious domain method in numerical simulation of an oscillating wave surge converter. Renew Energy 2018; 121: 133-145.
[17] Dias F, Van-Broeck JM. Nonlinear bow flows with spray. J Fluid Mech 1993; 255: 91-102.
[18] Sun SY, Sun SL, Ren HL, Wu GX. Splash jet and slamming generated by a rotating flap, Phys Fluids 2015; 27: 092107.
[19] Cheng Y, Li G, Ji CY, Zhai GJ. Numerical investigation of solitary wave slamming on an Oscillating Wave Surge Converter, Phys Fluids 2019; 31: 037102.
[20] Cheng Y, Li G, Ji CY, Zhai GJ. Solitary wave slamming on an Oscillating Wave Surge Converter over varying topography in the presence of collinear currents. Phys Fluids 2020; 32: 047102.
[21] Cheng Y, Ji CY, Zhai GJ. Fully nonlinear analysis incorporating viscous effects for hydrodynamics of an oscillating wave surge converter with nonlinear power take-off system, Energy, 2019;179:1067-1081.
[22] Babarit A. On the park effect in arrays of oscillating wave energy converters. Renew Energy 2013; 58: 68-78.
[23] Li YJ, Zhang CW. Analysis of wave resonance in gap between two heaving barges. Ocean Eng 2016; 17: 210-220.
[24] Kara F. Time domain prediction of power absorption from ocean waves with wave energy converter arrays. Renew Energy 2016; 92: 30-46.
[25] Nielsen SRK, Zhou Q, Basu B, Sichani MT, Kramer MM. Optimal control of an array of non-linear wave energy point converters. Ocean Eng 2014; 88: 242-254.
[26] Wei Y, Bechlenberg A, Van Rooij M, Jayawardhana B, Vakis AL. Modelling of a wave energy conver array with a nonlinear power take-off system in the frequency domain. Appl Ocean Res 2019; 90:101824.
[27] Wolgamot HA, Eatock Taylor R, Taylor PH. Effects of second-order hydrodynamics on the efficiency of a wave energy array. International Journal of Marine Energy 2016; 15: 85-99.
[28] Michele S, Renzi E. A second-order theory for an array of curved wave energy converters in open sea. J Fluid Struct 2019; 88: 315-330.
[29] Zhang H, Zhou B, Vogel C, Willden R, Zang J, Geng J. Hydrodynamic performance of a dual-floater hybrid system combining a floating breakwater and an oscillating-buoy type wave energy converter. Appl Energy, 2020, 259: 114212.
[30] Zhou BZ, Wu GX, Meng OC. Interactions of fully nonlinear solitary wave with a freely floating vertical cylinder. Eng Anal Bound Elem 2016; 69: 119-131.
[31] Zhong Q, Yeung RW. Wave-body interactions among energy absorbers in a wave farm. Appl Energy 2019; 233: 1051-1064.
[32] Fenton JD. A fifth order Stokes theory for steady waves. J Waterw Port Coast Ocean Eng ASCE 1985; 111: 216-234.